2018

Aerodynamics of Porous Bodies with Application to Aeroelastic Stability and Structural Acoustics

Rozhin Hajian
Lehigh University

Aerodynamics of Porous Bodies with Application to Aeroelastic Stability and Structural Acoustics

by

Rozhin Hajian

Presented to the Graduate and Research Committee

of Lehigh University

in Candidacy for the degree of

Doctor of Philosophy

in

Mechanical Engineering

Lehigh University

May 2018

Approved and recommended for acceptance as a dissertation in partial fulfillment of the requirements for the degree of Doctor of Philosophy.

Date

Accepted Date

Prof. Justin W. Jaworski
(Dissertation Advisor)

Committee Members:

Prof. Alparslan Oztekin

Prof. Keith W. Moored

Prof. Yue Yu

To all children without the right to education.

Acknowledgements

I would like to express my sincere gratitude and appreciation to my advisor, Professor Justin Jaworski, who made the journey possible and provided me with invaluable guidance, unfailing encouragement, and endless support. Despite his hectic schedule, he was always available for meetings and discussion. I could not be more grateful for having such a passionate and understanding advisor. Justin, thank you for making my Lehigh experience unique.

My gratitude also extends to the other members of my committee: Professors Oztekin, Moored, and Yu, for their help, advice, and constructive feedback. I would like to thank Professor Sheryl Grace and Dr. Lorna Ayton for all the fruitful discussions we had and their constant support. I would also like to express my gratitude to my master's advisor, Professor Nader Motee. Thank you for your endless support and for being an incredible mentor.

I would like to thank my friends and colleagues during the last four years. Fatma, Ihan, Steven, Tanya, Nate, and Emre, thank you for your friendship, encouragement, and creating a friendly and productive atmosphere in the office. I will never forget the experiences we have shared, and I hope to stay in touch. To all of my friends at DCDS lab, Shima, Yaser, Mirsaleh, Arash and Milad. You guys are the best!

I am grateful for the support of my amazing friends, Minoo, Tayeb, Rosa, and Amir!

Thank you for always being there for me. I am also delighted to have made incredible friendships during my graduate study. The friends I have made at Lehigh are too numerous to name. However, there are a few that cannot go unmentioned, Forough and Ebrahim, Jarfa, Alireza, Samane, PanteA, Bahar and Mohamad. You made this journey more enjoyable and fruitful for me, and I am incredibly glad to have each one of you in my life.

Much appreciation goes to the best parents I could have wished for, Fereshteh and Hassan. I would not be who am I today without you. I love you very much and thank you for all you have done for me, and specially for the best gifts of my life you gave me: my lovely sisters! Soma and Gelareh, and my brothers-in-law, Mahdi and Mohammad-Saeid, I am in debt to all of you for your love, support, and encouragement over these years.

Last but foremost, I would like to express my deepest gratitude to my soulmate and beloved husband, Milad. Thank you for always being there for me when life's challenges seemed too great to overcome, and for being supportive and patient when I was frustrated or completely lost. I can't thank you enough for your unconditional love and encouragement throughout this experience. Thank you for being in my life!

Contents

List of Tables

List of Figures

Abstract

The aerodynamic, aeroelastic, and acoustic implications of a prescribed porosity distribution on a thin airfoil or panel in a steady, two-dimensional, incompressible flow are formulated and solved in four distinct model problems. In pursuit of the steady aerodynamic loads on a porous airfoil, a Darcy porosity condition on the airfoil surface furnishes a Fredholm integral equation for the pressure distribution. This singular integral equation is solved exactly and generally as a Riemann-Hilbert problem provided that the porosity distribution is Hölder-continuous. The comparison between the new steady aerodynamic theory and experimental measurements of integrated lift forces on porous SD7003 airfoils in the literature shows good agreement for sufficiently small values of a dimensionless porosity parameter identified in the theoretical analysis.

The non-circulatory fluid forces are then derived on an oscillating porous panel or airfoil in a uniform incompressible flow. The fundamental integral equation for these unsteady loads resulting from a Darcy-type boundary condition with Hölder-continuous spatial distribution of porosity is formulated and solved in closed form as a Liouville-Neumann series. To demonstrate these analytical results, the non-circulatory pressure distributions for vibrating panels on simple or clamped supports with either uniform or variable chordwise porosity distributions are presented and compared.

These presented non-circulatory fluid forces are applied to aeroelastic stability predictions

for vibrating porous panels or liners fixed at both ends. Porous panels fixed at both ends lose aeroelastic stability by divergence, which is in agreement with the classical result for non-porous panels. However, the effect of porosity act to suppress divergence onset until higher flow speeds.

Finally, the acoustic far-field pressure is determined for a finite-chord panel with uniform porosity. The free space Green's function for the two-dimensional Helmholtz equation propagates the unsteady non-circulatory forces on the panel into the acoustic field. Results from this analysis identify the effects of varying the magnitude of a Darcy-type porosity condition on the acoustic emission of a vibrating panel in comparison to its non-porous counterpart. It is shown that the sound pressure produced by a uniformly-porous airfoil depends on the reduced frequency, Mach number, and the dimensionless porosity parameter. At low Mach numbers, increasing the magnitude of a Darcy-type porosity parameter leads to a reduction in the acoustic emission from a vibrating panel at high frequencies, while the introduction of porosity does not reduce the produced sound pressure at lower frequencies. Furthermore, it is demonstrated that, even at high frequencies, porosity does not always reduce the sound pressure; as the Mach number increases, larger values of the porosity parameter are required to reduce the sound generated from vibrating panels in all directions.

Chapter 1

Introduction

Inspired by silent flight of owls, a number of theoretical and experimental studies have been developed to predict the impact of the edge condition on the trailing-edge turbulence scattering mechanism [1–10]. These authors show that trailing-edge porosity and elasticity can be tuned to effectively eliminate the predominant scattering mechanism of trailing edge noise. However, the aerodynamic performance of a porous airfoil is expected to be worse than for a non-porous airfoil, where increasing the extent of the porous material decreases the lift and increases the drag [2, 9, 10]. Hence, there is a potential trade-off between the acoustical benefits of porosity and its negative impact on aerodynamic performance.

The central goal of this dissertation is to establish a theoretical basis to examine the effects of porosity on the aerodynamics, aeroelastic stability, and acoustic emission of airfoils and panels. To this end, each chapter herein addresses a defined modeling problem that builds upon the results of the previous chapters. Chapter 2 investigates the aerodynamic impact of a spatial variation in porosity distribution along the chordwise direction of stationary airfoils, where closed-form solutions are found by requiring only that the porosity distribution is Hölder continuous; Hölder continuity includes as a subset both

differentiable and piecewise-continuous classes of porosity distributions common to most airfoil designs of practical interest. Chapter 3 extends this work to include unsteady deformations of the panel section and presents an analytical expression for the non-circulatory pressure distribution on an arbitrarily-deforming panel with a prescribed chordwise porosity gradient. Chapters 4 and 5 apply the non-circulatory fluid forces defined in chapter 3 on a vibrating porous panel to study the aeroelastic stability for one-dimensional porous panels or liners that are fixed at both ends, and to predict the acoustic emission from vibrating porous panels in a single-sided flow, respectively.

Chapter 2

Steady aerodynamics of airfoils with porosity gradients

This chapter determines the aerodynamic loads on an airfoil with a prescribed porosity distribution in a steady incompressible flow. A Darcy porosity condition on the airfoil surface furnishes a Fredholm integral equation for the pressure distribution, which is solved exactly and generally as a Riemann-Hilbert problem provided that the porosity distribution is Hölder-continuous. The Hölder condition includes any differentiable and piecewise-continuous porosity distributions that may be of practical interest. This formal restriction on the analysis is examined by a class of differentiable porosity distributions that approach a piecewise, discontinuous function in a certain parametric limit. The Hölder-continuous solution is verified in this limit against analytical results for partially-porous airfoils in the literature. Finally, a comparison made between the new theoretical predictions and experimental measurements of SD7003 airfoils presented in the literature. Results from this analysis may be integrated into a theoretical framework to optimize turbulence noise suppression with minimal impact to aerodynamic performance.

2.1 Introduction

The study of aerodynamic loads on permeable airfoils can be motivated by the need for passive design structures to reduce the aerodynamic self-noise of fluid-loaded bodies. The trailing edge is an unavoidable source of this self-noise for aerodynamic structures and is the subject of a large body of research developed to model, measure, and mitigate the noise due to the edge interaction with turbulent eddies [3–8]. Turbulence noise can be reduced by changing the acoustical impedance near the edge [4]. A number of theoretical studies have sought to predict the impact of the edge boundary condition on the trailing-edge scattering mechanism. The seminal work of Ffowcs Williams and Hall [5] showed that the far-field acoustic intensity of a turbulent source in the presence of an impermeable rigid half plane is M^{-3} louder than a turbulent eddy in free space with no solid boundaries, where M is the eddy Mach number. Crighton and Leppington [11] confirmed this result using a different approach based on the Wiener-Hopf method and showed that a sufficiently limp edge scatters a weaker field of intensity M^{-2} louder than a free-space turbulent eddy; this Mach-number dependence is identical to the turbulence noise scaling of an edgeless perforated screen in the 'acoustically transparent' low-porosity limit identified by Ffowcs Williams [12]. Howe [6] also employed the Wiener-Hopf method to predict the scattered field from an elastic edge, including its critical dependence on the coincidence frequency. Using the poroelastic plate model of Howe [7], Jaworski and Peake [8] examined the scattering of turbulent noise sources from a poroelastic half-plane. Motivated by the unique wing attributes of silent owl species, these authors showed that trailing-edge porosity and elasticity can be tuned to effectively eliminate the predominant scattering mechanism of trailing edge noise. Recent analytical work by Ayton [13] extended these results to examine the effects of finite chord for partially-porous airfoils. Also, Cavalieri *et al.* [14] developed a boundary element framework to investigate the

elasticity and porosity of finite-chord airfoils on the scattered acoustic field, noting the complementary noise reduction in high and low frequency ranges due to elasticity and porosity effects, respectively. The aforementioned works consider only stationary bodies and represent porosity with the Rayleigh conductivity of a thin perforated surface, which neglects any viscous effects within the pores. Weidenfeld and Manela [15] predicted that porous noise reductions can indeed persist when a viscous Darcy porosity condition is applied to a pitching airfoil. However, to be useful in the design of any practical application, these aeroacoustic works need a complementary assessment of porosity on the aerodynamics.

The generalized airfoil aerodynamic theory of Woods [16] considered the aerodynamics of porous foils in inviscid, steady, and subsonic flow, where the pressure jump across the wall of a hollowed airfoil was linearly related to the local normal flow velocity. However, in contrast to the present study and passive porous airfoil experiments considered herein, Woods assumed a prescribed pressure distribution along the interior surface of the airfoil, whereas here the upper and lower surfaces of the airfoil communicate through the Darcy boundary condition. The Darcy boundary condition holds for small Reynolds numbers based upon the pore permeability and seepage velocity [15] and is tacitly assumed to be valid in the analysis herein. From intuition and according to measurements by Geyer *et al.* [9, 10], the aerodynamic performance of a porous airfoil is expected to be worse than for a non-porous airfoil, where an increase in the extent of the porous material decreases the lift and increases the drag. Numerical computations by Bae and Moon [17] corroborate these trends, demonstrate the ability of porous trailing edges to suppress tonal peaks in the acoustic signature, and suggest that the optimization of the porosity distribution could enable greater noise reductions, e.g. [18]. Hence, there is a potential trade-off between the acoustical benefits of porosity and its negative impact on

aerodynamic performance. Recent experimental work by Geyer and Sarradj [10] investigated the aerodynamic noise from airfoils with a finite-length porous trailing edge in an effort to incorporate the acoustic advantages of porosity. Geyer and Sarradj [10] showed that, depending on the porous material, airfoils with porosity at the trailing-edge section only can still lead to a noticeable noise reduction, while maintaining a certain level of aerodynamic performance over a fully-porous airfoil. The impact of a finite region of uniform porosity along the aft portion of airfoil has been examined theoretically by Iosilevskii [1, 2], resulting in closed-form expressions for pressure distribution, lift and pitching-moment coefficients, and seepage drag of the airfoil. However, it is unknown what impact a *variation* in porosity distribution would have on the airfoil performance, which may be optimized for noise suppression in conjunction with an external aeroacoustic analysis.

This chapter defines the impact of a functional porosity gradient on the steady aerodynamics of an airfoil. The fundamental singular integral equation is derived and solved exactly for the broad class of Hölder-continuous porosity distributions. The resulting general expression for the pressure distribution may be evaluated numerically and is evaluated in chapter 2.4 in closed form for the special case of uniform porosity. Furthermore, analytical and numerical evaluations of this general result in the limit of a discontinuous porosity jump are demonstrated to match the analytical work of Iosilevskii [1]. Lastly, the pressure distribution for a porous SD7003 airfoil is integrated to furnish a lift prediction, which is compared and contrasted against the experimental data of Geyer *et al.* [9]. The results presented in this chapter have been published in [19].

2.2 Mathematical model

Consider a thin airfoil under the assumption of small disturbances in a two-dimensional, steady incompressible flow. The solution to the flow field may be written as the linear combination of two velocity potential functions [20],

$$\phi = \phi^t + \phi^l, \tag{2.1}$$

where ϕ^t denotes the flow field correction due to airfoil thickness, and ϕ^l is the lifting flow field due to airfoil camber and angle of attack. The symmetry of the thickness problem requires the same pressure distribution above and below the airfoil, and thus no pressure jump exists across the airfoil. This fact holds regardless of whether or not the airfoil is porous. Therefore, porosity does not affect the solution of the thickness problem presented in the classical literature [20,21]. However, the thickness of a generalized porous airfoil can be absorbed into the porosity distribution function and is represented in the lifting problem [22]. The lifting problem is now formulated and solved.

Suppose a mean background flow velocity oriented in the x-direction such that $\mathbf{U} = U\hat{i}$, and the local flow rate, w_s, directed along the unit normal to the airfoil surface, $\hat{n} = (-\frac{\partial z_a}{\partial x}, 1)$, is given by

$$\begin{aligned} w_s &= (\nabla\phi + \mathbf{U}) \cdot \hat{n} \\ &= \Big(\frac{\partial\phi}{\partial x} + U, \frac{\partial\phi}{\partial z}\Big) \cdot \Big(-\frac{dz}{dx}, 1\Big) \\ &= -\frac{\partial\phi}{\partial x}\frac{dz}{dx} - U\frac{dz}{dx} + \frac{\partial\phi}{\partial z}. \end{aligned} \tag{2.2}$$

Classical linear aerodynamic theory requires the ratios of the flow perturbation velocities relative to U and the local slope of the airfoil to be small [23], say, $O(\lambda)$, such that

$O(\lambda^2)$ terms are neglected. (Note that this ordering scheme permits the present analysis to hold for weakly-compressible flows provided that the Mach number is also $O(\lambda)$. The interested reader may wish to consult Van Dyke [24] and references therein for consideration of Mach number expansions, which are not pursued in detail here.) After neglecting higher-order terms, (2.2) becomes

$$w(x,z) = w_s + U\frac{dz}{dx}, \tag{2.3}$$

where $w(x,z) = \partial\phi/\partial z$. The perturbed flow velocity in the field is also related to the bound vorticity distribution on the airfoil, $\gamma(x)$, by [23]

$$w(x,z) = -\frac{1}{2\pi}\int_{-1}^{1}\frac{(x-\xi)\gamma(\xi)}{(x-\xi)^2+z^2}d\xi, \tag{2.4}$$

where x and z have been non-dimensionalized by the airfoil semi-chord. For an airfoil with a nondimensional Darcy-type porosity distribution $R(x)$, the local flow rate is linearly proportional to the porosity and vorticity distribution [25]:

$$w_s = \rho UCR(x)\gamma(x). \tag{2.5}$$

The combination of equations (2.3-2.5) evaluated at the airfoil surface ($z = 0$) furnishes a Fredholm integral equation for the vorticity distribution,

$$2\rho UCR(x)\gamma(x) - \frac{1}{\pi}\fint_{-1}^{1}\frac{\gamma(t)}{t-x}dt = -2U\frac{dz}{dx}, \tag{2.6}$$

where constants ρ, U, and C define the air density, mean flow velocity, and the porosity coefficient, respectively. The function $z(x)$ defines the camber line of the wing, *e.g.*, for a flat airfoil at angle of attack α, $dz/dx = -\alpha$.

The dimensionless pressure jump is linearly related to the vorticity distribution by [23]

$$p(x) \;=\; \frac{p_u(x) - p_l(x)}{\frac{1}{2}\rho U^2} \;=\; -\,2\frac{\gamma(x)}{U}, \tag{2.7}$$

where p_u and p_l denote the dimensional pressure distributions above and below the wing.

According to the Darcy boundary condition, the local flow velocity directed along the unit normal to the airfoil surface is

$$w_s = -\frac{\zeta}{\mu n d}(p_u - p_l), \tag{2.8}$$

where ζ, μ, n, and d denote the permeability of the solid porous medium, the dynamic viscosity of the fluid, the open area fraction of the porous material, and the thickness of the airfoil, respectively. For real airfoils in ordinary scenarios, the values of ζ, μ, and n are constant, but the thickness $d = d(x)$ varies along the chord.

Also, equations (2.5) and (2.7) together yield:

$$w_s = -CR(x)(p_u - p_l). \tag{2.9}$$

Therefore, we can define the multiplication of the porosity coefficient, C, and porosity distribution, $R(x)$, based on the physical properties of the airfoil and surrounding fluid as follows:

$$CR(x) = \frac{\zeta}{\mu n d}. \tag{2.10}$$

By substitution of (2.7) into (2.6), the following integral equation is obtained:

$$\rho U C R(x) p(x) - \frac{1}{2\pi}\fint_{-1}^{1} \frac{p(t)}{t - x}dt \;=\; 2\frac{dz}{dx}. \tag{2.11}$$

Equation (2.11) has been non-dimensionalized using U and $\frac{1}{2}\rho U^2$ as the velocity and pressure scales. This integral equation is identical to that examined by Iosilevskii, equation (9) in [2] with a change of variable $\epsilon = \rho UC$ and $R(x) = H(x-a)$, where $H(x)$ is the Heaviside function and a is the chordwise location where the non-porous and uniformly-porous segments meet. The class of singular integral equations with Cauchy kernels in the form of (2.11) can be formulated and solved as a Riemann-Hilbert problem [26, 27].

2.3 Solution of the airfoil pressure distribution

The integral equation (2.11) is now solved as a Riemann-Hilbert problem. Comparing (2.11) with the canonical singular integral equation (47.1) in [26],

$$A(x)p(x) + \frac{B(x)}{\pi i}\int_L \frac{p(t)}{t-x}dt = f(x), \tag{2.12}$$

we have

$$A(x) = \delta R(x) = \frac{\psi(x)}{2}, \quad B(x) = -\frac{i}{2}, \quad f(x) = 2\frac{dz}{dx}, \tag{2.13}$$

where the dimensionless parameter $\delta = \rho UC$ embodies the interaction between fluid and airfoil porosity, while $\psi(x) = 2\delta R(x)$ contains the airfoil geometry effects as well. Note that L is a smooth contour that contains points t and x, and $A(x)$, $B(x)$ are functions given on L. To make progress, the following assumptions must be satisfied [26]:

1. The line L consists of a finite number of (smooth) non-intersecting contours, which is here a single open contour from -1 to 1 on the real axis.

2. The functions $A(x)$ and $B(x)$ must be Hölder-continuous. A function h is Hölder-

continuous when there are non-negative real constants α and β such that the relation

$$|h(x) - h(y)| \leq \alpha |x - y|^{\beta} \tag{2.14}$$

holds everywhere on L.

3. The sum and difference functions $S(x) = A(x) + B(x)$ and $D(x) = A(x) - B(x)$ do not vanish anywhere on L.

The index κ of the Fredholm integral equation (2.11) is identically zero, $\kappa \equiv 0$ [26, 28].

The general solution for the pressure distribution on an airfoil with a Hölder-continuous porosity distribution $R(x)$ is now pursued. Following the procedure of [26], define the set of auxiliary functions

$$G(x) = \frac{A(x) - B(x)}{A(x) + B(x)} = \frac{\psi(x) + i}{\psi(x) - i}, \tag{2.15}$$

$$\Gamma(x) = \frac{1}{2\pi i} \fint_{-1}^{1} \frac{\log G(t)}{t - x} dt = \fint_{-1}^{1} \frac{k(\psi(t))}{t - x} dt, \tag{2.16}$$

to obtain the fundamental function $Z(x)$,

$$Z(x) = \sqrt{A^2(x) - B^2(x)}\, x^{-\kappa/2} e^{\Gamma(x)} \tag{2.17}$$

$$= \frac{\sqrt{1 + \psi^2(x)}}{2} \exp\Big(\fint_{-1}^{1} \frac{k(\psi(t))}{t - x} dt \Big), \tag{2.18}$$

where $k(\psi(x)) = \frac{1}{\pi} \cot^{-1} \psi(x)$ for real $\psi(x)$.

Substitution of equations (4.22-4.24) into the general solution given by (47.13) in [26] yields

$$p(x) = A^*(x) f(x) - \frac{B^*(x) Z(x)}{\pi i} \fint_{-1}^{1} \frac{f(t) dt}{Z(t)(t - x)} + B^*(x) Z(x) P_{\kappa - 1}(x), \tag{2.19}$$

where $P_{\kappa-1}(x)$ is an arbitrary polynomial of degree not greater than $\kappa-1$ ($P_{\kappa-1}(x)\equiv 0$ for $\kappa=0$), and

$$A^*(x) = \frac{A(x)}{A^2(x)-B^2(x)} = \frac{2\psi(x)}{1+\psi^2(x)}, \tag{2.20}$$

$$B^*(x) = \frac{B(x)}{A^2(x)-B^2(x)} = \frac{-2i}{1+\psi^2(x)}. \tag{2.21}$$

Finally, the substitution of equations (4.26, 4.27) into (4.25) gives the following pressure distribution for an airfoil with the prescribed porosity distribution $R(x)$:

$$\begin{aligned} p(x) &= \frac{4\psi(x)}{1+\psi^2(x)}\frac{dz}{dx} \\ &- \frac{4}{\pi\sqrt{1+\psi^2(x)}}\exp\left(\fint_{-1}^{1}\frac{k(\psi(t))}{t-x}dt\right) \\ &\times \fint_{-1}^{1}\frac{dz/dt}{\sqrt{1+\psi^2(t)}\exp\left(\fint_{-1}^{1}\frac{k(\psi(\xi))}{\xi-t}d\xi\right)(x-t)}dt. \end{aligned} \tag{2.22}$$

Recall that $\psi(x) = 2\rho UCR(x)$ and $k(\psi(x)) = \frac{1}{\pi}\cot^{-1}\psi(x)$ for real $\psi(x)$. Equation (2.22) supplies the pressure jump across a thin airfoil with any Darcy-type porosity distribution, provided that this distribution is Hölder-continuous. We note that the Hölder condition includes any differentiable and piecewise-continuous porosity distributions that may be of practical interest.

In general, (2.22) must be evaluated numerically, but analytical progress can be made for a uniformly-porous airfoil. In the next section, the general solution (2.22) furnishes closed-form expressions for the pressure distribution over a uniformly-porous airfoil. The theoretical result (2.22) is also shown to hold in the discontinuous limit of a partially-porous airfoil, where the Hölder continuity condition formally breaks down.

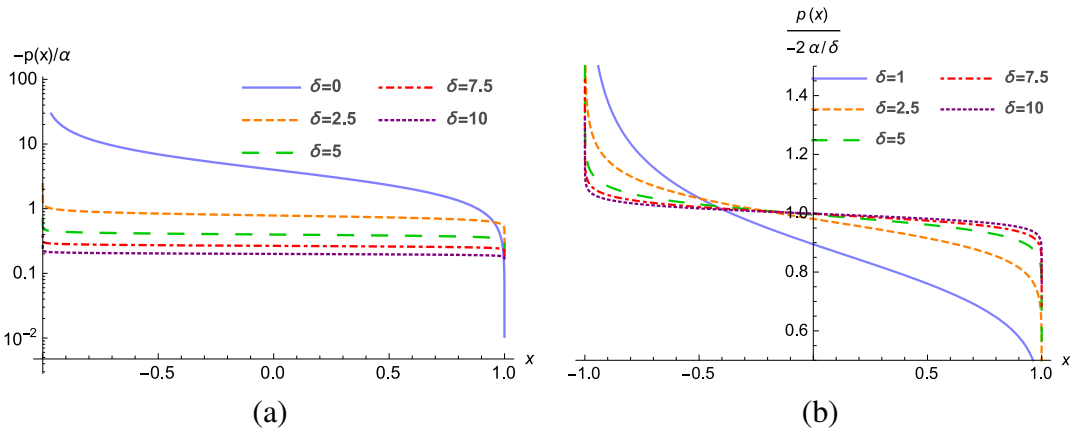

(a) (b)

Figure 2.1: Normalized pressure distribution of a uniformly-porous flat airfoil for different porosity parameters δ: (a) pressure jump normalized by angle of attack, $-p(x)/\alpha$; (b) pressure jump normalized by the high porosity limit, $-p(x)/(2\alpha/\delta)$.

2.4 Special cases

In this section, the general solution (2.22) is demonstrated for airfoils with uniform porosity, and for partially-porous airfoils composed of a non-porous leading-edge section attached to a trailing-edge section of uniform porosity.

2.4.1 Uniformly-porous airfoils

For the uniformly-porous airfoil, $R(x) = 1$ and $\psi = 2\delta$ is a constant. Therefore, (4.23) becomes

$$\Gamma(x) \;=\; k(2\delta)\int_{-1}^{1}\frac{dt}{t-x} = \ln\left(\frac{1-x}{1+x}\right)^{k(2\delta)}, \tag{2.23}$$

and the pressure distribution obtained by (2.22) can be written in the following form:

$$p(x) \;=\; \frac{8\delta}{1+4\delta^2}\frac{dz}{dx} - \frac{4}{\pi(1+4\delta^2)}\left(\frac{1-x}{1+x}\right)^{k(2\delta)}\int_{-1}^{1}\frac{dz/dt}{x-t}\left(\frac{1+t}{1-t}\right)^{k(2\delta)}dt. \tag{2.24}$$

This result holds generally for any camber line $z(x)$. However, if we restrict ourselves to a flat airfoil at angle of attack α, such that $dz/dx = -\alpha$, then the pressure distribution is

$$p(x) = \frac{-4\alpha}{\sqrt{1+4\delta^2}}\Big(\frac{1-x}{1+x}\Big)^{k(2\delta)}. \tag{2.25}$$

The obtained pressure distribution (2.25) for the uniformly-porous airfoil is the same as the result of Iosilevskii [1] for an airfoil with constant porosity that was determined using an independent asymptotic approach. According to (2.25), increasing the porosity parameter decreases the pressure distribution over the uniform-porosity airfoil, as illustrated in figure 2.1(a). For $\delta \gg 1$, the pressure distribution becomes increasingly flat with the value

$$p(x) \sim \frac{-2\alpha}{\delta}, \tag{2.26}$$

and all of the substantial variations in pressure jump are shifted closer to the leading and trailing edges. This trend can be seen in the pressure distributions normalized by the high porosity limit (2.26) shown in figure 2.1(b). Note that the singular behavior of the normalized pressure jump near the leading edge ($x \to -1$) in this case is

$$p(x) \sim \frac{-2^{k(2\delta)+2}\alpha}{\sqrt{1+4\delta^2}}(1+x)^{-k(2\delta)}, \tag{2.27}$$

while the regular behavior near the trailing edge ($x \to 1$) is approximated by

$$p(x) \sim \frac{-2^{-k(2\delta)+2}\alpha}{\sqrt{1+4\delta^2}}(1-x)^{k(2\delta)}. \tag{2.28}$$

The limiting case of a non-porous airfoil, where the porosity coefficient $C = 0$ and

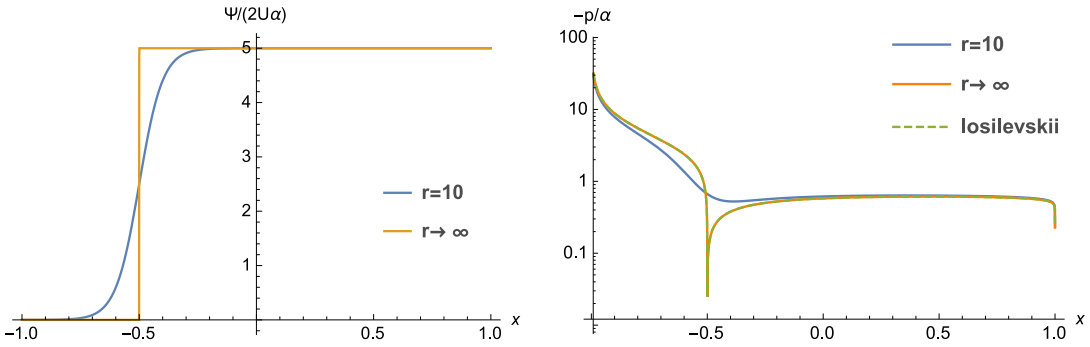

(a) (b)

Figure 2.2: Porosity and pressure distributions of a thin airfoil with a prescribed differentiable porosity distribution given by (2.30) with $a = -0.5$: (a) porosity distributions for $r = 10$ and $r \to \infty$;
(b) pressure distributions for $r = 10$ and the singular limit as $r \to \infty$ for the flat airfoil. The dashed line indicates Iosilevskii's result, equation (13) in [1].

$k(0) = 1/2$, recovers the well-known pressure distribution for a non-porous airfoil [23]:

$$p(x) = -4\alpha\sqrt{\frac{1-x}{1+x}}. \tag{2.29}$$

Note that all integrated loads such as lift, pitching moment, and seepage drag can be determined for the uniformly-porous airfoil from the pressure distribution provided by (2.24).

2.4.2 Partially-porous airfoils

The general result (2.22) for a generic Hölder-continuous porosity distribution is now demonstrated to also hold in the discontinuous limit of a partially-porous thin airfoil. The aerodynamic impact of a finite, uniform porosity distribution along the aft portion of an airfoil has been examined theoretically by Iosilevskii [1, 2], resulting in closed-form expressions for pressure distribution, lift and pitching-moment coefficients, and seepage drag of the airfoil, which can be reproduced numerically in the discontinuous limit of

a continuous porosity distribution. Attention is again given below only to the pressure distribution, from which all of the aerodynamic coefficients can be derived.

Suppose a thin airfoil with the following prescribed differentiable porosity distribution (cf. [15, 29]):

$$\frac{\psi(x)}{2\rho U} = CR(x) = \frac{1}{2}C\Big(1 + \tanh[r(x-a)]\Big). \tag{2.30}$$

The porosity distribution given in (2.30) is differentiable and therefore automatically Hölder-continuous, and the general solution (2.22) for the pressure distribution is valid. We note that $\tanh[r(x-a)] \to \pm 1$ as $r \to \infty$ for $x \gtrless a$, enabling the pressure distribution (2.22) to be written in the following form in the case of a thin airfoil with parabolic camber line, in which $dz/dx = -\alpha - \beta x$, as $r \to \infty$:

$$\begin{aligned} p(x) &= \frac{-4(\alpha+\beta x)\psi(x)}{1+\psi^2(x)} \\ &+ \frac{4}{\pi\sqrt{1+\psi^2(x)}}\left|\frac{a-x}{1+x}\right|^{\frac{1}{2}}\left|\frac{1-x}{a-x}\right|^{\frac{\cot^{-1}C}{\pi}} \\ &\times \int_{-1}^{1}\frac{\alpha+\beta t}{\sqrt{1+\psi^2(t)}(x-t)}\left|\frac{1+t}{a-t}\right|^{\frac{1}{2}}\left|\frac{a-t}{1-t}\right|^{\frac{\cot^{-1}C}{\pi}} dt, \end{aligned} \tag{2.31}$$

where

$$\frac{\psi(x)}{2\rho U} \to \begin{cases} 0 & \text{for } x < a, \\ C & \text{for } x > a. \end{cases} \tag{2.32}$$

From (2.32), note that as $r \to \infty$ the airfoil with given porosity distribution (2.30) represents a partially-porous thin airfoil, composed of an impermeable forward segment connected to an aft permeable section with a constant porosity distribution. Figure 2.2 illustrates the porosity distribution (2.30) for the illustrated case of $a = -0.5$ with $r = 10, \infty$ and the resulting pressure distribution for a flat airfoil ($\beta = 0$). In the limit $r \to \infty$,

the present model is validated by the independent asymptotic analysis of Iosilevskii [1] for partially-porous airfoils.

Note that the porosity distribution (2.30) is an example of a Hölder-continuous function that behaves as a discontinuous piecewise function in the limit $r \to \infty$ to represent a partially-porous airfoil. Other types of functions, e.g. piecewise continuous functions among others, may be used to attain the same result.

2.5 Comparison with experimental data for porous SD7003 airfoils

This section compares and contrasts the obtained theoretical result for lift coefficient using the pressure distribution (2.22) against experimental measurements by Geyer *et al.* [9] of airfoils constructed of uniform porous material at various flow speeds U. The chord-based Reynolds number varies between approximately 4×10^5 and 8×10^5, and the Mach number lies in the range of $0.07 - 0.14$. Their experimental study cut slabs of porous textiles into a modified semi-symmetrical SD7003 airfoil shape. This process was repeated to create a set of airfoils, each of which was constructed using a single textile. Each textile has an intrinsic air flow resistivity, r, which can be measured from a static pressure drop test of a uniform slab of material using [9]

$$r = \frac{\Delta p}{w_s d}, \tag{2.33}$$

where Δp and d denote the pressure drop and the thickness of the porous sample, respectively. According to the theoretical model and equation (2.33), the porosity coefficient, C, and porosity distribution, $R(x)$, can be written in terms of the flow resistivity of the

textile and the thickness distribution of the SD7003 airfoil section:

$$C = \frac{1}{r}, \qquad R(x) = \frac{1}{d(x)}. \tag{2.34}$$

The slope of the camber line, dz/dx, and thickness distribution, $d(x)$, of the SD7003 airfoil are represented in the theoretical model by curve fits to airfoil coordinate data in [30]. These curves are based upon standard formulae describing NACA airfoils and are presented in Appendix A.

In the experimental study, airfoils are placed in an open jet wind tunnel such that its spanwise extent is greater than the nozzle diameter, which is circular and of Witoszynski type. In an attempt to make a comparison with the present theoretical model, the measured lift force, F_L, on the wing is converted into a lift coefficient,

$$c_L = \frac{F_L}{\frac{1}{2}\rho U^2 l S}, \tag{2.35}$$

where l and S denote the chord length and estimated wetted wing span, respectively.

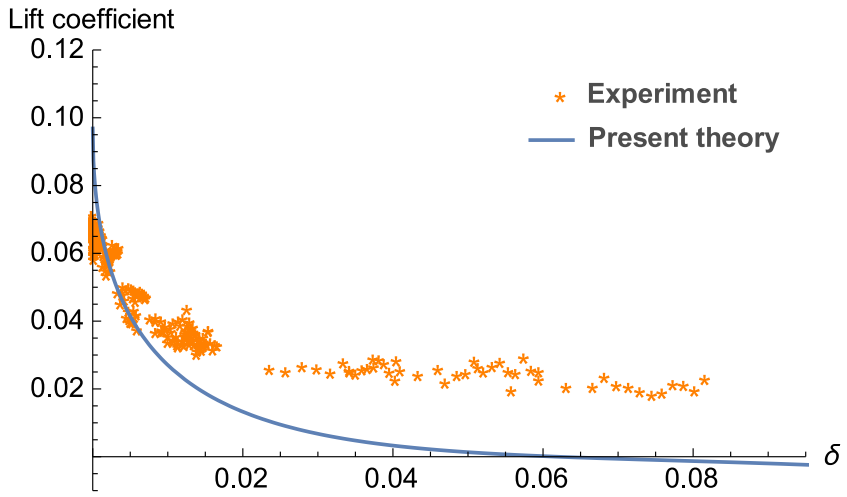

Figure 2.3: Comparison of the predicted and measured lift coefficients of a porous SD7003 airfoil at zero angle of attack for various porosity constants δ.

Figure 2.3 compares the predicted and measured lift coefficients of a porous SD7003 airfoil at zero angle of attack with various physical porosity properties. The lift coefficient measured experimentally for the non-porous airfoil ($\delta = 0$), $c_L \simeq 0.07$, is less than the expected value based on the theory, $c_L = 0.0974$. One would not expect these numbers to match exactly, as Geyer *et al.* [9] themselves indicated that angle-of-attack corrections to their raw lift data were abandoned due to their experimental configuration. However, both theory and experiment show qualitatively that the lift coefficient decreases with increasing porosity parameter δ as expected. For small δ, the experimental measurements agree well with the theoretical model, and changes to the lift coefficient become less sensitive to the porosity parameter as it increases. For porosity parameter values above the approximate value $\delta \approx 0.01$ the theoretical predictions and the experimental data diverge: the experiments yield a positive lift for all δ considered, yet the model predicts negative lift at large δ. This latter trend suggests that there may be a predominant physical flow feature of porous airfoils with high porosity values that is not considered by the present model. High porosity values may invalidate the small pore-based Reynolds number restriction required by the Darcy boundary condition and the merit the investigation of more general porosity laws, such as the Ergun model [17,31]. The sensitivity of the aerodynamic loads to the choice of porosity boundary condition at large δ is beyond the scope of the present work and is the subject of ongoing research.

In the theoretical model, we observe the change to negative lift coefficient and reverse pressure distribution after some porosity parametric value δ_0, which depends on the mean camber line of the airfoil. As it is shown in figure 2.4, the singular pressure distribution at the leading edge starts from positive infinity, dips to negative values away from the leading edge, and then changes sign at a point ahead of the trailing edge. The location of the sign change moves toward the trailing edge as the porosity parameter δ increases.

Note that the lift coefficient remains negative for large porosity constants. Therefore, for any cambered airfoil there is a porosity constant δ_0 beyond which the airfoil produces a negative lift coefficient for $\delta > \delta_0$. The change of sign in the pressure distribution occurs due to the airfoil camber, as discussed in Appendix B for the uniformly porous special case. Porous symmetric airfoils at positive angle of attack maintain a positive pressure distribution and integrated lift for all porosity parameters.

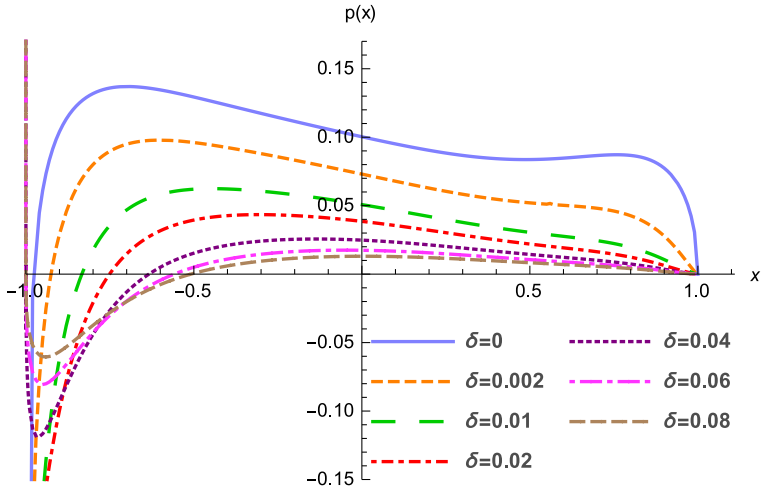

Figure 2.4: Pressure distribution of a porous SD7003 airfoil at zero angle of attack for various porosity constants δ, based on the theoretical model.

2.6 Chapter summary

This chapter presents the exact solution for the pressure distribution over an airfoil in a steady incompressible flow with a prescribed Hölder-continuous porosity distribution. Aerodynamic loads coefficients, lift, moment coefficients, and seepage drag can be obtained in closed form for the special case of a uniformly-porous airfoil. Previous analytical results for partially-porous airfoils are recovered by the new general solution for certain limiting cases of piecewise-continuous and differentiable porosity distributions,

which further verifies the present results. A comparison of the lift prediction for a porous SD7003 airfoil against available experimental data indicates good agreement for sufficiently small values of the nondimensional porosity parameter that depends on the flow and porosity of the airfoil material. For large values of the porosity parameter the model predicts negative lift, a phenomenon due to the camber of porous airfoils and not the angle of attack. Experimental data at large porosity parameter values are positive for all available data and suggest a missing physical feature in the present model at these high porosity cases that is the subject of future investigation. Further extensions of the current work could also include unsteady airfoil motions, which would rely on the general solution of (2.6), where the theoretical frameworks of Theodorsen [32] and Jaworski [33] could be appropriate.

Chapter 3

Non-circulatory fluid forces on panels and airfoils with porosity gradients

The non-circulatory fluid forces on an oscillating porous panel or airfoil in a uniform incompressible flow are derived from linearized potential theory. The fundamental integral equation resulting from a Darcy-type boundary condition with Hölder-continuous spatial distribution of porosity is formulated and solved. To demonstrate these analytical results, the non-circulatory pressure distributions for vibrating panels on simple or clamped supports with either uniform or variable chordwise porosity distributions are presented and compared. Results from this analysis enable the future aeroelastic stability calculation for flexible, perforated panels and aim to form the basis of a complete unsteady aerodynamic and vortex-sound theories for porous airfoils based upon the unique attributes of natural fliers and swimmers.

3.1 Introduction

The classical theory of Theodorsen [32] and its later extensions [33] developed closed-form expressions for the unsteady aerodynamic forces on a piecewise-continuous rigid and impermeable airfoil undergoing small-amplitude harmonic motions in a uniform incompressible flow. These analyses separated the total fluid forces or moments into circulatory and non-circulatory parts, which correspond respectively to the contribution of the unsteady shedding of vorticity into the wake and the non-lifting hydrodynamic sloshing of fluid about the airfoil [23]. Following the same approach, Gaunaa [34] developed a general theoretical framework to predict the aerodynamic loads on unsteady thin deformable airfoils. These unsteady fluid forces also contribute fundamentally to the airfoil gust response problem [23, 35] and the aerodynamic noise generation due to vortex-structure interactions [36].

The aerodynamic theory of non-circulatory forces on moving bodies in a steady flow has previously been studied for impermeable flexible panels with various leading- and trailing-edge boundary conditions in both supersonic and subsonic flows [37–43]. Accordingly, the mode of instability depends on the boundary conditions as well as the Mach number. This chapter contributes to this literature by furnishing the aerodynamic loads on an oscillating porous panel to enable aeroelastic stability predictions, which will be discussed later in chapter 4.

The present chapter extends the steady analysis of chapter 2 to determine the unsteady non-circulatory forces on an arbitrarily deforming panel with a Hölder-continuous porosity distribution [44]. An analytical expression for the non-circulatory pressure distribution is presented and evaluated for the special cases of uniform and variable-porosity panels undergoing harmonic deformations. These results constitute the first major step towards a complete linearized, unsteady aerodynamic theory for lifting porous bodies, which may

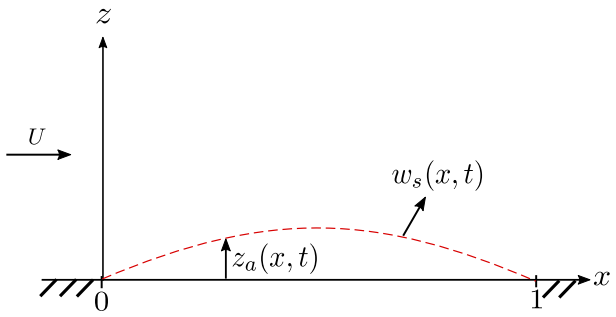

Figure 3.1: Schematic of a thin, porous panel in one-sided flow of speed U, undergoing unsteady deformations $z_a(x,t)$ and with seepage velocity $w_s(x,t)$.

have potential application to the performance estimation of biologically-inspired swimmers and fliers and to the future assessment of aeroelastic stability and flow noise production of porous airfoils.

3.2 Mathematical model

Consider a thin panel or airfoil undergoing prescribed unsteady motions in a two-dimensional steady, incompressible flow. For non-circulatory forces, it is sufficient to consider the baffled panel with single-sided flow illustrated in figure 3.1, as neither a vortex sheet nor the Kutta condition are imposed here. Supposing a chord length l, mean flow speed U, and fluid density ρ, all terms are nondimensionalized using l, l/U, and $\frac{1}{2}\rho U^2$ as the length, time, and pressure scales, respectively.

3.2.1 Porous boundary condition

In the problem illustrated in figure 3.1, the background flow velocity and the panel deflection can be written as $\mathbf{U}_{\text{flow}} = U\hat{i}$ and $\mathbf{U}_{\text{panel}} = Dz_a/Dt\,\hat{k}$, respectively, where D/Dt denotes the total derivative, and the function $z_a(x,t)$ defines the mean surface of the airfoil or deforming panel. To obtain the two-dimensional boundary condition along a porous

airfoil, consider the local seepage flow rate directed along the unit normal to the airfoil surface, w_s,

$$w_s \;=\; (\nabla\phi + \mathbf{U}_{\text{flow}} - \mathbf{U}_{\text{panel}}) \cdot \hat{n}, \tag{3.1}$$

where ϕ is the perturbation velocity potential. The linearized normal unit vector is $\hat{n} = (-\frac{\partial z_a}{\partial x}, 1)$, and the perturbation flow velocity on the airfoil surface is

$$w(x,t) = w_s + \frac{\partial z_a}{\partial x} + \frac{\partial z_a}{\partial t}, \tag{3.2}$$

where $w(x,t) = \partial\phi/\partial z|_{z=0}$. For an airfoil with a Darcy-type porosity distribution, the local flow rate is linearly proportional to the porosity and dimensionless pressure distribution: [19, 25]

$$w_s = f_0(p(x,t)) = -\frac{1}{2}\rho U C R(x) p(x,t), \tag{3.3}$$

where C is the porosity coefficient, $R(x)$ is a dimensionless function defining the porosity distribution, and $p(x,t)$ is the dimensionless pressure jump (upper minus lower) across the panel. Comparison of the relationship between the local pressure jump and seepage velocity w_s against the standard Darcy boundary condition [45] allows the product $CR(x)$ to be defined in terms of physical parameters the same as in (2.10). Recall that the symbol μ denotes the fluid viscosity, and κ, n, and d represent the permeability, open area fraction, and thickness of the porous material, respectively, all which may vary with chordwise location x.

3.2.2 Derivation of the singular integral equation

The non-circulatory flow about the panel can be represented by a distribution of sources and sinks just above and below the line $z = 0$, which furnishes the following non-dimensional disturbance potential [23]:

$$\phi(x,z,t) = \frac{1}{2\pi}\int_0^1 w(\xi,t)\ln[(x-\xi)^2+z^2]d\xi, \tag{3.4}$$

where $w(x,t)$ is given by (5.10). The linearized Bernoulli equation relates the dimensionless pressure jump to the dimensionless disturbance potential evaluated at $z = 0^+$ by [23]

$$p(x,t) = -2\left(\frac{\partial\phi}{\partial x}+\frac{\partial\phi}{\partial t}\right). \tag{3.5}$$

The combination of (5.10-3.5) produces a singular integral equation of the second kind:

$$\begin{aligned} p(x,t) &= \frac{1}{2\pi}\left(\fint_0^1 \frac{\psi(\xi)p(\xi,t)}{x-\xi}d\xi + \frac{\partial}{\partial t}\int_0^1 \psi(\xi)p(\xi,t)\ln|x-\xi|d\xi\right) \\ &\quad +O(x,t), \end{aligned} \tag{3.6}$$

where

$$\psi(x) = 2\rho UCR(x), \tag{3.7}$$

$$O(x,t) = -\frac{2}{\pi}\left(\fint_0^1 \frac{g(\xi,t)}{x-\xi}d\xi + \frac{\partial}{\partial t}\int_0^1 g(\xi,t)\ln|x-\xi|d\xi\right), \tag{3.8}$$

$$g(x,t) = \frac{\partial z_a}{\partial x}+\frac{\partial z_a}{\partial t}. \tag{3.9}$$

These equations recover the result derived by Kornecki *et al.* [39] in the special case of impermeable panels ($C = 0$). However, for porous panels, (3.6) depends on both x and

t and cannot be solved directly in its present form. Application of a Fourier transform in time yields the ordinary singular integral equation

$$\hat{p}(x) + \frac{\psi(x)}{2\pi}\int_0^1 \frac{\hat{p}(\xi)}{\xi - x}d\xi + \frac{1}{\pi i}\int_0^1 k(x,\xi)\hat{p}(\xi)d\xi = \hat{O}(x), \tag{3.10}$$

where

$$\begin{aligned}\hat{O}(x) \quad &= -\frac{2}{\pi}\int_0^1 \frac{d\hat{z}_a}{d\xi}\left(i\omega \ln|x-\xi| + \frac{1}{x-\xi}\right)d\xi \\ &\quad -\frac{2i\omega}{\pi}\int_0^1 \hat{z}_a\left(i\omega \ln|x-\xi| + \frac{1}{x-\xi}\right)d\xi,\end{aligned} \tag{3.11}$$

$$k(x,\xi) = \frac{\omega}{2}\psi(\xi)\ln|x-\xi| + \frac{i}{2}\frac{\psi(\xi)-\psi(x)}{\xi - x}, \tag{3.12}$$

and the hats denote transformed functions. A comparison of (3.10) with the canonical singular integral equation (57.1) in Muskhelishvili [26] identifies a set of auxiliary functions that enable an analytical solution:

$$G(x) = \frac{2 - i\psi(x)}{2 + i\psi(x)}, \tag{3.13}$$

$$\begin{aligned}\Gamma(x) &= \frac{1}{2\pi i}\int_0^1 \frac{\log G(t)}{t-x}dt, \\ &= \frac{-1}{\pi}\int_0^1 \frac{\tan^{-1}[\psi(\xi)/2]}{\xi - x}d\xi,\end{aligned} \tag{3.14}$$

$$Z(x) = \sqrt{1 + \frac{\psi^2(x)}{4}}\, e^{\Gamma(x)}. \tag{3.15}$$

Finally, (3.10) can be recast into the form:

$$\hat{p}(x) \quad + \quad \frac{1}{\pi i}\int_0^1 N(x,\xi)\hat{p}(\xi)d\xi = \frac{4}{4+\psi^2(x)}\hat{O}(x) - \frac{\psi(x)}{\pi\sqrt{4+\psi^2(x)}}$$

$$\times \exp\left(-\frac{1}{\pi}\fint_0^1 \frac{\tan^{-1}(\psi(t)/2)}{t-x}dt\right)\fint_0^1 \frac{\hat{O}(t)}{Z(t)(t-x)}dt, \tag{3.16}$$

where

$$\begin{aligned} N(x,\xi) &= \frac{4}{4+\psi^2(x)}k(x,\xi) - \frac{\psi(x)}{\pi\sqrt{4+\psi^2(x)}} \\ &\quad \times \exp\left(-\frac{1}{\pi}\fint_0^1 \frac{\tan^{-1}(\psi(t)/2)}{t-x}dt\right)\fint_{-1}^1 \frac{k(t,\xi)}{Z(t)(t-x)}dt. \end{aligned} \tag{3.17}$$

Equation (3.16) is a Fredholm integral equation of the second kind, which may be solved using a Liouville-Neumann series [46]. To complete the analysis, the inverse Fourier transform of the solution to (3.16) determines the non-circulatory pressure distribution for an arbitrary panel deformation history.

The next section pursues the solution of porous panels undergoing harmonic motions with a single frequency, from which a Fourier series in time may be used to construct the unsteady pressure distribution on panels with an arbitrary deformation history.

3.3 Solution for porous panels undergoing harmonic motions

The non-circulatory fluid forces are now studied for porous panels or airfoils with harmonic motions, such that $z_a(x,t) = X(x)e^{i\omega_0 t}$ and $p(x,t) = P(x)e^{i\omega_0 t}$, where $P(x)$ is a complex-valued function and ω_0 is a dimensionless frequency. The integral equation (3.6) can now be reduced and rearranged into the canonical form

$$P(x) + \frac{1}{\pi i}\fint_0^1 N(x,\xi)P(\xi)d\xi = f(x), \tag{3.18}$$

where

$$
\begin{aligned}
N(x,\xi) &= \frac{k(x,\xi)}{1+\delta^2R^2(x)} - \frac{\delta R(x)}{\pi\sqrt{1+\delta^2R^2(x)}}e^{\Gamma(x)} \\
&\quad \times \fint_0^1 \frac{k(y,\xi)}{\sqrt{1+\delta^2R^2(y)}e^{\Gamma(y)}(y-x)}dy, \qquad (3.19) \\
f(x) &= \frac{O(x)}{1+\delta^2R^2(x)} - \frac{\delta R(x)}{\pi\sqrt{1+\delta^2R^2(x)}}e^{\Gamma(x)} \\
&\quad \times \fint_0^1 \frac{O(y)}{\sqrt{1+\delta^2R^2(y)}e^{\Gamma(y)}(y-x)}dy, \qquad (3.20)
\end{aligned}
$$

and (4.6, 3.12) reduce to

$$
\begin{aligned}
O(x) &= \frac{2}{\pi}\fint_0^1 \frac{X'(\xi)+i\omega_0X(\xi)}{\xi-x}d\xi \\
&\quad -\frac{2i\omega_0}{\pi}\int_0^1 [X'(\xi)+i\omega_0X(\xi)]\ln|x-\xi|d\xi, \qquad (3.21) \\
k(x,\xi) &= \omega_0\delta R(\xi)\ln|x-\xi| + i\delta\frac{R(\xi)-R(x)}{\xi-x}. \qquad (3.22)
\end{aligned}
$$

Here $\delta = \rho UC$ is a constant, and $\Gamma(x)$ is again defined by (3.14).

The solution to (4.14) can be written as a Liouville-Neumann series [46],

$$
P(x) = \lim_{n\to\infty}\sum_{k=0}^{n}\lambda^k u_k(x), \qquad (3.23)
$$

where $\lambda = -1/\pi i$ and

$$
\begin{aligned}
u_0(x) &= f(x), \qquad (3.24) \\
u_1(x) &= \fint_0^1 N(x,\xi_1)f(\xi_1)d\xi_1, \\
&\vdots
\end{aligned}
$$

$$u_n(x) \;=\; \fint_0^1 \cdots \fint_0^1 N(x,\xi_1)N(\xi_1,\xi_2)\cdots N(\xi_{n-1},\xi_n)f(\xi_n)d\xi_n\cdots d\xi_1.$$

Expressions (4.17) and (3.24) together constitute the general solution for the non-circulatory pressure distribution over a porous panel or airfoil with porosity distribution $R(x)$ undergoing harmonic oscillations in a single-sided flow.

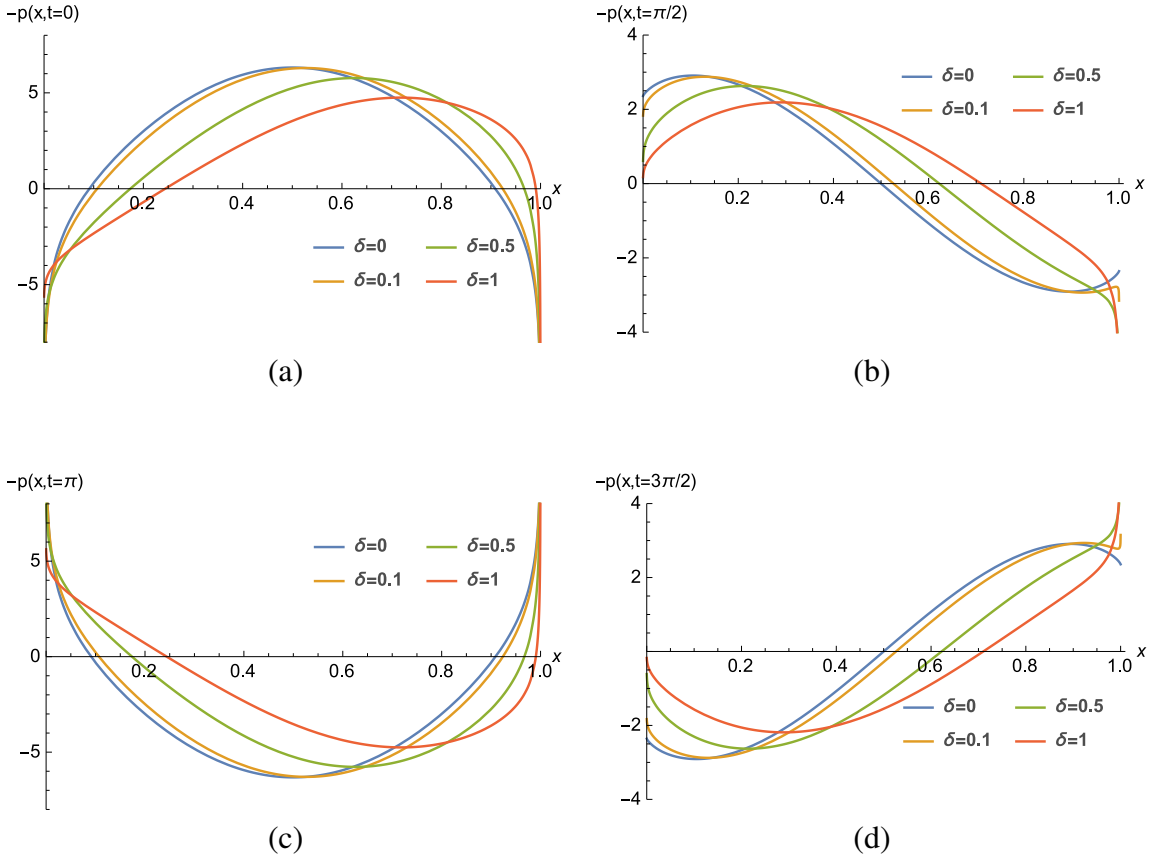

Figure 3.2: Pressure distribution for simply-supported non-porous and uniformly-porous panels with $X(x) = \sin(\pi x)$ and $\omega_0 = 1$ at different instants in time: (a) $t = 0$, (b) $t = \pi/2$, (c) $t = \pi$, and (d) $t = 3\pi/2$.

For uniformly-porous panels and airfoils, $R(x) = 1$ and $\psi = 2\delta$ is a constant. Therefore, the associated non-circulatory fluid forces for this uniformly-porous bodies with

harmonic movements can be determined from (4.17) with

$$N(x,\xi) = \frac{\omega_0\delta}{1+\delta^2}\ln|x-\xi| - \frac{\omega_0\delta^2}{\pi(1+\delta^2)}\left(\frac{x}{1-x}\right)^{\frac{1}{\pi}\tan^{-1}\delta} \times\!\!\!\!\!\!\int_0^1 \frac{\ln|y-\xi|}{y-x}\left(\frac{1-y}{y}\right)^{\frac{1}{\pi}\tan^{-1}\delta} dy \tag{3.25}$$

and

$$f(x) = \frac{O(x)}{1+\delta^2} - \frac{\delta}{\pi(1+\delta^2)}\left(\frac{x}{1-x}\right)^{\frac{1}{\pi}\tan^{-1}\delta} \int_0^1 \frac{O(\xi)}{\xi-x}\left(\frac{1-\xi}{\xi}\right)^{\frac{1}{\pi}\tan^{-1}\delta} d\xi. \tag{3.26}$$

Note that the Liouville-Neumann series is not strictly ordered based on the smallness of the porosity parameter δ, and the first term of the series, $u_0(x) = f(x)$, incorporates the effects of porosity. It is further noted that the Liouville-Neumann series converges rapidly for small porosity values of aerospace interest, as will be discussed in the next section.

3.4 Discussion

The solution for a panel vibrating at a single frequency (4.17) is now evaluated numerically to examine the effects of panel shape and chordwise variation in porosity on the non-circulatory pressure distribution. The examples presented here use sinusoidal or quartic panel shapes to approximate the deformations of a panel on simple or clamped supports, respectively, and the results for a square-root porosity gradient are compared against the case of uniform porosity. The numerical results presented involve only the leading-order term $P(x) \approx u_0(x) = f(x)$ in the solution, as the remaining terms are typically orders of magnitude smaller in practice. The magnitude of the second term in the Liouville-Neumann series relative to the first term is $O(10^{-1})$ when $\delta = 1$, which de-

creases to $O(10^{-3})$ when $\delta = 0.1$. Note that expected values of the porosity parameter in low-speed applications are $\delta = O(10^{-2})$, as measured experimentally by Geyer *et al.* [9] and analyzed by Hajian and Jaworski [19]. The pressure distributions for δ values of this magnitude do not show appreciable differences when compared to the non-porous case. Therefore, larger values of δ are considered here to illustrate the effects of increasing porosity on the pressure distribution more clearly.

Figures 3.2 and 3.3 show the real part of the pressure solution $p(x,t) = P(x)e^{i\omega_0 t}$ for non-porous and uniformly-porous panels at $\omega_0 = 1$ and compare the effects of a sinusoidal panel displacement $X(x) = \sin \pi x$ representative of simple end supports against one that is clamped at both ends, as described by $X(x) = 16(x^4 - 2x^3 + x^2)$. In both cases, the aerodynamic pressure distributions on non-porous panels ($\delta = 0$) are symmetric about the mid-chord at $t = 0$. Figures 3.2 and 3.3 both indicate that the introduction of porosity breaks the left-right symmetry of the pressure distribution at $t = 0$, reduces the pressure peak, and shifts the peak location towards the trailing edge for increasing values of the porosity parameter δ. These observations are reinforced when the panel deformation is viewed in continuous time in figure 3.4. It is generally observed that the non-circulatory pressure distribution on uniformly-porous panels retains the singular or regular behavior of their non-porous counterpart at the leading edge. A singular behavior always occurs for uniformly-porous panels at the trailing edge; this singularity at $x = 1$ arises from the second term of $f(x)$ in (5.12) for $\delta > 0$. The non-circulatory pressure distribution over the clamped panel in figure 3.3 is regular at the leading edge for all instants of time shown. However, figure 3.2 indicates a leading-edge singularity for the simple-supported panel at times $t = 0$ and $t = \pi$.

Figure 3.5 compares the numerical results for the pressure distribution over a non-porous panel, uniformly-porous panel ($\delta = 0.5$), as well as a panel with porosity distribu-

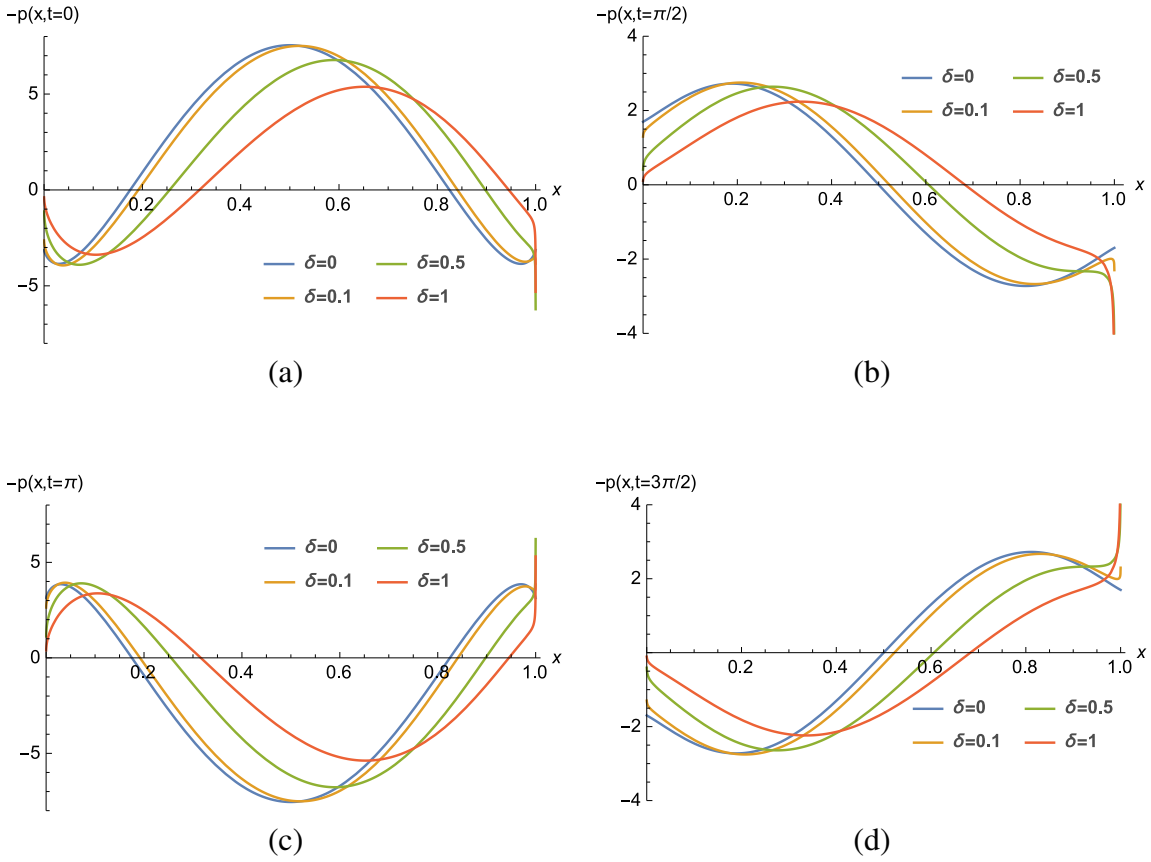

Figure 3.3: Pressure distribution for the non-porous and uniformly-porous panels clamped at both ends with displacement of $X(x) = 16(x^4 - 2x^3 + x^2)$, and $\omega_0 = 1$ at different instants in time: (a) $t = 0$, (b) $t = \pi/2$, (c) $t = \pi$, and (d) $t = 3\pi/2$.

tion $R(x) = 1 - \sqrt{x}$ with $\delta = 0.5$; these cases are all produced for $\omega_0 = 1$ with sinusoidal panel deformations $X(x) = \sin \pi x$ at different instants in time. Similar to the uniform porosity results above, the introduction of a porosity gradient along the chord also breaks the left-right symmetry of the pressure distribution at $t = 0$, reduces the pressure peak, and shifts the peak location towards the trailing edge. However, the reduction in the pressure peak and magnitude of the shift of the peak location in the variable porosity panel is less than for the uniformly-porous panel. At the leading edge, the singular behavior of the non-porous panel at $t = 0$ and $t = \pi$ is retained in the variable porosity case, as is the regular behavior at $t = \pi/2$ and $t = 3\pi/2$. However, in contrast to the uniformly-porous

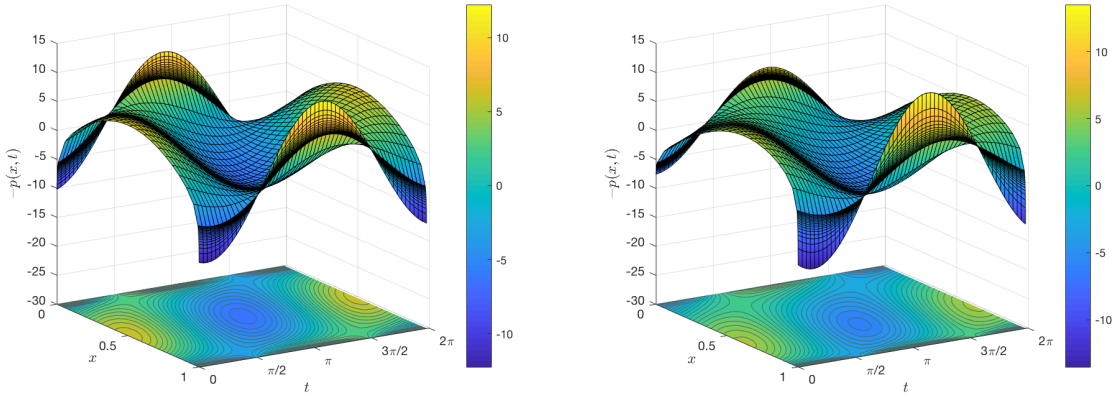

(a) (b)

Figure 3.4: Periodic non-circulatory pressure distribution $p(x,t)$ over one period with sinusoidal panel waveform $X(x) = \sin(\pi x)$ and $\omega_0 = 1$: (a) non-porous panel, (b) uniformly-porous panel with $\delta = 0.5$.

case, a panel with the given porosity gradient behaves like a non-porous panel at the trailing edge and does not generate a singularity there. This regular behavior is obtained here by choosing a porosity function that vanishes at the trailing edge, i.e. $R(1) = 0$.

3.5 Chapter summary

From linearized aerodynamic theory, a Fredholm integral equation is derived and solved analytically as a Liouville-Neumann series for the non-circulatory pressure distribution on an oscillating porous panel or airfoil in a uniform incompressible flow. The fundamental integral equation results from the application of a Darcy-type porosity boundary condition that has a Hölder-continuous spatial distribution along the chord. The pressure distribution is determined explicitly for the case of a single frequency, which can be used to determine the pressure distribution resulting from arbitrary panel deformations with a Fourier series in time.

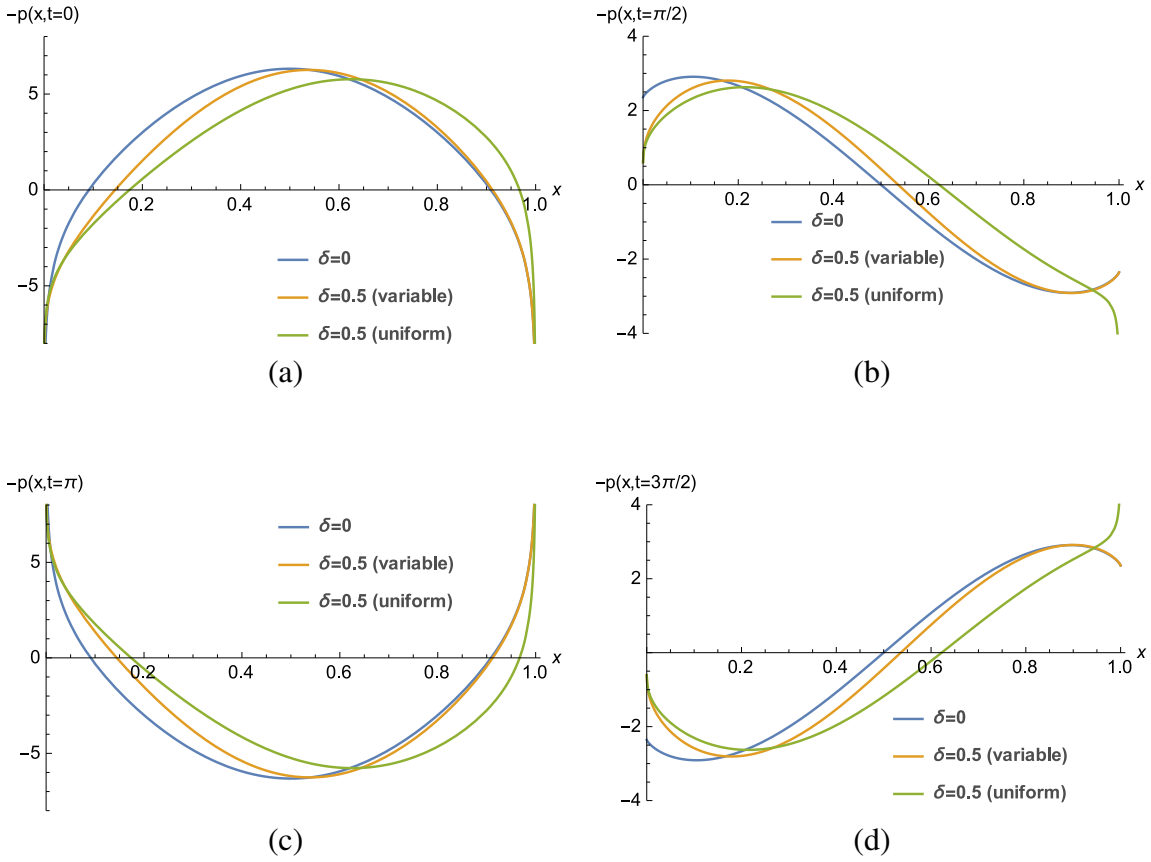

Figure 3.5: Comparison of non-circulatory pressure distributions for non-porous, uniformly-porous, and variable porosity panels with $R(x) = 1 - \sqrt{x}$ and $\delta = 0.5$, with a simply support of $X(x) = \sin(\pi x)$ and $\omega_0 = 1$ at different instants in time: (a) $t = 0$, (b) $t = \pi/2$, (c) $t = \pi$, and (d) $t = 3\pi/2$.

To demonstrate these analytical results, the non-circulatory pressure distributions for vibrating panels on simple or clamped supports with either uniform or variable chordwise porosity distributions are presented and compared. Porosity breaks the well-known left-right symmetry of the non-porous pressure distribution, reduces the pressure peak, and shifts the peak location towards the trailing edge for increasing values of the porosity parameter δ. The magnitude and aftward shift of the peak is affected by the prescribed chordwise porosity gradient. The non-circulatory pressure distribution over the clamped panel is regular at the leading edge for all time instants considered, but a simply-supported

panel with sinusoidal displacement generates a pressure singularity at the leading edge. At the leading edge, porous panels retain the singular or regular behavior of their non-porous counterpart. A singular behavior is always observed at the trailing edge for porous panels, with the exception of cases where the porosity vanishes at the trailing edge. The choice of a porosity function that vanishes at the trailing edge recovers the regular behavior of the pressure field observed for non-porous panels. Results from this analysis are anticipated to enable future aeroelastic stability calculations for flexible, perforated panels and to form a more complete theoretical basis to study the unsteady aerodynamics and noise generation of porous structures based upon the unique attributes of natural fliers and swimmers.

Chapter 4

Aeroelastic instability of porous panels with fixed ends

The non-circulatory fluid forces on an oscillating porous panel are applied to aeroelastic stability predictions for porous panels or liners, fixed at both ends. It is shown that a porous panel with fixed ends loses its stability by divergence, which is in agreement with the classical result for non-porous panels. However, the divergence speed of porous panel is greater than its value for non-porous panels, and the divergence speed increases monotonically with increasing porosity parameter.

4.1 Introduction

Vibrating panels are common sound sources in many engineering devices, such as passively-tuned vibration absorbers (TVA) [47,48], and continue to be the subject of active research [49, 50]. The introduction of a mean flow adjacent to a flexible panel introduces the possibility of self-excited vibrations resulting from aeroelastic flutter. For one-dimensional panels fixed at each edge, the flutter boundary may be calculated using a set of appropriate

structured equations coupled to non-circulatory aerodynamic theory. The non-circulatory forces in a steady flow have been previously studied for vibrating, flexible panels with different boundary conditions at the leading and trailing edges for both supersonic and subsonic flows [37–43, 51, 52]. Accordingly, the type of aeroelastic instability depends on the boundary conditions and on the Mach number. In subsonic flow, panels fixed at both ends lose stability primarily by divergence, which has been studied both theoretically [37–39, 51, 52] and experimentally [38, 52]. For example, Dugundji *et al.* [52] showed that divergence occurs for a simply-supported panel at a lower flow speed than for flutter. However, Weaver and Unny [51] demonstrated that the critical flow speeds for divergence and flutter might be close together numerically, where one could imagine in a physical experiment that the primary divergence instability is accidentally bypassed and flutter oscillations of the secondary instability are observed instead. Flutter can be the true primary instability type in the case of other boundary conditions, such as cantilevered ends [39, 42], which has been confirmed experimentally [39]. Similar results have been also obtained for an elastic strip pinned at one end and free at the other [42].

The present chapter contributes to the panel flutter literature by incorporating the effects of panel porosity into aeroelastic stability predictions. In this chapter, the unsteady aerodynamic loads on oscillating panels developed in chapter 3 are coupled to a structural equation of motion to furnish aeroelastic stability predictions for porous panels or liners fixed at both ends. The introduction of porosity to the flexible panel is shown to not change the primary mode of instability: divergence. However, the critical velocity at which an aeroelastic instability occurs is demonstrated to be larger for the porous panels than their non-porous counterparts.

4.2 Mathematical model

This section presents the structural and aerodynamic equations used to study the aeroelastic instability of a thin panel in a two-dimensional steady, incompressible flow, as illustrated in figure 3.1. First, the linear equation of panel deformation is presented and nondimensionalized. The non-circulatory aerodynamic forces are then coupled to the panel elastic motion to investigate the aeroelastic stability of porous panels.

4.2.1 Governing equation of panel motion

According to the Euler-Lagrange equation [53], the applied load on a dynamic one-dimensional panel with linear deformations $\bar{z}_a(x,t)$ is related to the deflection by

$$q = D\frac{\partial^4 \bar{z}_a}{\partial \bar{x}^4} + \rho_s h \frac{\partial^2 \bar{z}_a}{\partial \bar{t}^2}, \tag{4.1}$$

where D, ρ_s, and h denote the flexural rigidity, mass density, and panel thickness, respectively. Therefore, a one-dimensional, fluid-loaded panel satisfies

$$D\frac{\partial^4 \bar{z}_a}{\partial \bar{x}^4} + \rho_s h \frac{\partial^2 \bar{z}_a}{\partial \bar{t}^2} + (p_u - p_l) = 0. \tag{4.2}$$

The terms p_u and p_l represent the local pressures above and below the panel, respectively. All parameters in (4.2) are dimensional. By introducing the non-dimensional variables $x = \bar{x}/l$, $z_a = \bar{z}_a/l$, and $t = \bar{t}/\sqrt{\rho_s h l^4/D}$, (4.2) can be written in the following form:

$$\frac{\partial^4 z_a}{\partial x^4} + \frac{\partial^2 z_a}{\partial t^2} + \frac{\lambda^2}{2} p(x,t) = 0, \tag{4.3}$$

where $\lambda^2 = \rho U^2 l^3/D$, and $p(x,t)$ denotes the dimensionless pressure jump (upper minus lower) across the panel.

4.2.2 Non-circulatory pressure distribution

Consider a thin panel or airfoil undergoing prescribed unsteady motions in a two-dimensional steady, incompressible flow, as shown in figure 3.1. For harmonic motions of impermeable airfoils, the classical work of Theodorsen [23, 32] separates the fluid forces into circulatory and non-circulatory parts, which are related to the unsteady shedding of vorticity into the wake and the hydrodynamic sloshing of fluid about the airfoil, respectively. Theodorsen's approach was adopted in chapter 3 to the unsteady motions of porous panels and determine the non-circulatory contribution for a panel with a prescribed porosity distribution. In the problem illustrated in figure 3.1, the background flow velocity and the panel deflection can be written as $\mathbf{U}_{\text{flow}} = U\hat{i}$ and $\mathbf{U}_{\text{panel}} = Dz_a/Dt\,\hat{k}$, respectively, where D/Dt denotes the total derivative. We recall the following singular integral equation, which had been derived in chapter 3 for the non-circulatory pressure distribution over a panel with porosity distribution $R(x)$:

$$\begin{aligned} p(x,t) &= \frac{1}{2\pi}\left(\fint_0^1 \frac{\psi(\xi)p(\xi,t)}{x-\xi}d\xi + \frac{\sqrt{\mu_m}}{\lambda}\frac{\partial}{\partial t}\int_0^1 \psi(\xi)p(\xi,t)\ln|x-\xi|d\xi\right) \\ &\quad + O(x,t), \end{aligned} \tag{4.4}$$

where

$$\psi(x) = 2\rho UCR(x), \tag{4.5}$$

$$O(x,t) = -\frac{2}{\pi}\left(\fint_0^1 \frac{g(\xi,t)}{x-\xi}d\xi + \frac{\sqrt{\mu_m}}{\lambda}\frac{\partial}{\partial t}\int_0^1 g(\xi,t)\ln|x-\xi|d\xi\right), \tag{4.6}$$

$$g(x,t) = \frac{\partial z_a}{\partial x} + \frac{\sqrt{\mu_m}}{\lambda}\frac{\partial z_a}{\partial t}. \tag{4.7}$$

In these equations, $\mu_m = \rho l/\rho_s h$, and C is the porosity coefficient. Comparison of the relationship between the local pressure jump and seepage velocity w_s against the standard

Darcy boundary condition [45] allows the product $CR(x)$ to be defined in terms of physical parameters the same as in (2.10). Recall that the symbol μ denotes the fluid viscosity, and κ, n, and d represent the permeability, open area fraction, and thickness of the porous material, respectively, all which may vary with chordwise location x.

4.2.3 Formation of generalized aeroelastic divergence problem

According to prior theoretical investigations [37, 38], non-porous panels with both ends fixed lose stability initially via divergence. The critical flow velocity at which divergence occurs can be found by analyzing the panel static stability under steady aerodynamic forces [39]. However, further analysis is needed to show that divergence is the primary form of instability for porous panels, which will be discussed in more detail in the next section. To study the divergence for porous panels, the time dependence may be dropped from (4.4), which leads to the following integral equation for the critical pressure distribution:

$$p_{\text{cr}}(x) = \frac{1}{2\pi}\int_0^1 \frac{\psi(\xi)p_{\text{cr}}(\xi)}{x-\xi}d\xi - \frac{2}{\pi}\int_0^1 \frac{\partial z_a/\partial\xi}{x-\xi}d\xi. \tag{4.8}$$

This expression can be recast into the following canonical form that admits a general solution:

$$p_{\text{cr}}(x) + \frac{\psi(x)}{2\pi}\int_0^1 \frac{p_{\text{cr}}(\xi)}{\xi-x}d\xi + \frac{1}{\pi i}\int_0^1 k(x,\xi)p_{\text{cr}}(\xi)d\xi = \frac{2}{\pi}y(x), \tag{4.9}$$

where

$$k(x,\xi) = \frac{i}{2}\frac{\psi(\xi)-\psi(x)}{\xi-x}, \tag{4.10}$$

and

$$y(x) = \int_0^1 \frac{\partial z_a/\partial \xi}{\xi - x} d\xi = z_a'(1)\ln(1-x) - z_a'(0)\ln(x) - \int_0^1 \frac{\partial^2 z_a}{\partial \xi^2} \ln|\xi - x| d\xi. \tag{4.11}$$

A comparison of (4.9) with the canonical singular integral equation (57.1) in Muskhelishvili [26] identifies a set of auxiliary functions that enable an analytical solution:

$$\begin{aligned} A^*(x) &= \frac{4}{\psi^2 + 4}, \\ B^*(x) &= \frac{2\psi i}{\psi^2 + 4}, \\ G(x) &= \frac{-2/\psi + i}{-2/\psi - i}, \\ \Gamma(x) &= \frac{1}{2\pi i}\int_0^1 \frac{\log(G(x))}{\xi - x} d\xi, \end{aligned} \tag{4.12}$$

and the fundamental function Z is given by

$$Z(x) = \sqrt{1 + \frac{\psi^2}{4^2}}\, e^{\Gamma(x)}. \tag{4.13}$$

Finally, the singular integral equation (4.9) can be written in the following form of a Fredholm integral equation of second kind:

$$p_{\text{cr}}(x) + \frac{1}{\pi i}\int_{-1}^1 N(x,\xi) p_{\text{cr}}(\xi) d\xi = f(x), \tag{4.14}$$

where

$$N(x,\xi) = \frac{-i}{2(1+\psi(x)^2/4)} \frac{\psi(\xi) - \psi(x)}{\xi - x} - \frac{i\psi(x)}{4\pi\sqrt{1+\psi(x)^2/4}} e^{\Gamma(x)} \int_0^1 \frac{\psi(\xi) - \psi(t)}{(\xi - t)\sqrt{1+\psi(t)^2/4}} e^{-\Gamma(t)} \frac{dt}{t - x}, \tag{4.15}$$

and

$$f(x) = \frac{8/\pi}{\psi(x)^2+4}\, y(x) - \frac{4\psi(x)}{\pi^2\sqrt{\psi(x)^2+4}} e^{\Gamma(x)} \fint_0^1 \frac{y(t)}{\sqrt{\psi(t)^2+4}(t-x)} e^{-\Gamma(t)} dt. \quad (4.16)$$

The solution of Fredholm integral equation of the second kind (4.14) can be written as a Liouville-Neumann series:

$$p_{\text{cr}}(x) = \lim_{n\to\infty} p_n(x) = \lim_{n\to\infty} \sum_{i=0}^{n} \xi^i u_i(x), \quad (4.17)$$

where $\xi = -1/\pi i$, and

$$\begin{aligned} u_0(x) &= f(x), \quad (4.18)\\ u_1(x) &= \fint_{-1}^{1} N(x,t_1) f(t_1) dt_1, \\ &\vdots \\ u_n(x) &= \fint_{-1}^{1}\fint_{-1}^{1}\fint_{-1}^{1} N(x,t_1)N(t_1,t_2)\cdots N(t_{n-1},t_n) f(t_n) dt_n \cdots dt_1. \end{aligned}$$

As discussed in chapter 3, the Liouville-Neumann series converges rapidly for small porosity values of aerospace interest. Therefore, the solution of (4.17) is approximated by the first term of the series, u_0, and

$$\begin{aligned} p_{\text{cr}}(x) \approx\ & \frac{8/\pi}{\psi(x)^2+4}\, y(x) \quad (4.19)\\ & - \frac{4\psi(x)}{\pi^2\sqrt{\psi(x)^2+4}} e^{\Gamma(x)} \fint_0^1 \frac{y(\xi)}{(\xi-x)\sqrt{\psi(\xi)^2+4}} e^{-\Gamma(\xi)} d\xi. \end{aligned}$$

To obtain the critical flow velocity, (4.19) is substituted into the equation of panel motion (4.3). Considering only the static stability under steady aerodynamic forces, reduces

the panel motion equation to

$$\frac{d^4 z_a}{dx^4} + \frac{\lambda^2}{\pi}\Big(\frac{y(x)}{1+\psi(x)^2/4} + \frac{\psi(x)}{2\pi\sqrt{1+\psi(x)^2/4}} e^{\Gamma(x)} \times \int_0^1 \frac{y(\xi)}{(\xi - x)\sqrt{1+\psi(\xi)^2/4}} e^{-\Gamma(\xi)} d\xi\Big) = 0. \quad (4.20)$$

The special case of (4.20) for non-porous panels ($\psi = 0$) recovers the result derived previously by Kornecki *et al*, (cf. (14) in [39]).

4.3 Aeroelastic instability of uniformly-porous panels

This section studies the aeroelastic instability of uniformly-porous panels, for which $R(x) = 1$ and $\psi = 2\delta$ is a constant.

4.3.1 Divergence instability

For uniformly-porous panels, (4.8) can be recast in the following form:

$$p_{\text{cr}}(x) + \frac{\delta}{\pi}\int_0^1 \frac{p_{\text{cr}}(\xi)}{\xi - x} d\xi = \frac{2}{\pi}\int_0^1 \frac{\partial z_a/\partial \xi}{\xi - x} d\xi, \quad (4.21)$$

where $\delta = \rho U C$. Following the procedure described in [26], a set of auxiliary functions may be defined as follows:

$$G(x) = \frac{A(x) - B(x)}{A(x) + B(x)} = \frac{1 - \delta i}{1 + \delta i}, \quad (4.22)$$

$$\Gamma(x) = \frac{1}{2\pi i}\int_{-1}^1 \frac{\log G(t)}{t - x} dt = -k(\delta) \ln\Big(\frac{1-x}{x}\Big), \quad (4.23)$$

where $k(\delta) = (\tan^{-1}\delta)/\pi$ for real δ, and the fundamental function $Z(x)$ is given by

$$\begin{aligned} Z(x) &= \sqrt{A^2(x) - B^2(x)}\, x^{-\kappa/2} e^{\Gamma(x)} \\ &= \frac{\sqrt{1+\delta^2}}{2}\Big(\frac{x}{1-x}\Big)^{k(\delta)}. \end{aligned} \tag{4.24}$$

Substitution of equations (4.22)-(4.24) into the general solution given by (47.13) in [26] yields

$$p(x) = A^*(x)f(x) - \frac{B^*(x)Z(x)}{\pi i}\fint_{-1}^{1} \frac{f(t)dt}{Z(t)(t-x)} + B^*(x)Z(x)P_{\kappa-1}(x), \tag{4.25}$$

where $P_{\kappa-1}(x)$ is an arbitrary polynomial of degree not greater than $\kappa - 1$ ($P_{\kappa-1}(x) \equiv 0$ for $\kappa = 0$), and

$$A^*(x) = \frac{A(x)}{A^2(x) - B^2(x)} = \frac{1}{1+\delta^2}, \tag{4.26}$$

$$B^*(x) = \frac{B(x)}{A^2(x) - B^2(x)} = \frac{i\delta}{1+\delta^2}. \tag{4.27}$$

Finally, the substitution of (4.26) and (4.27) into (4.25) yields the following $p_{\text{cr}}(x)$ for uniformly-porous panels:

$$p_{\text{cr}}(x) = \frac{f(x)}{1+\delta^2} - \frac{\delta}{\pi(1+\delta)^2}\Big(\frac{x}{1-x}\Big)^{k(\delta)} \fint_0^1 \frac{f(\xi)}{\xi - x}\Big(\frac{1-\xi}{\xi}\Big)^{k(\delta)} d\xi, \tag{4.28}$$

where

$$\begin{aligned} f(x) &= \frac{2}{\pi}\fint_0^1 \frac{\partial z_a/\partial\xi}{\xi - x} d\xi \\ &= \frac{2}{\pi}\Big(z_a'(1)\ln(1-x) - z_a'(0)\ln(x) - \int_0^1 \frac{\partial^2 z_a}{\partial \xi^2}\ln|\xi - x| d\xi\Big). \end{aligned} \tag{4.29}$$

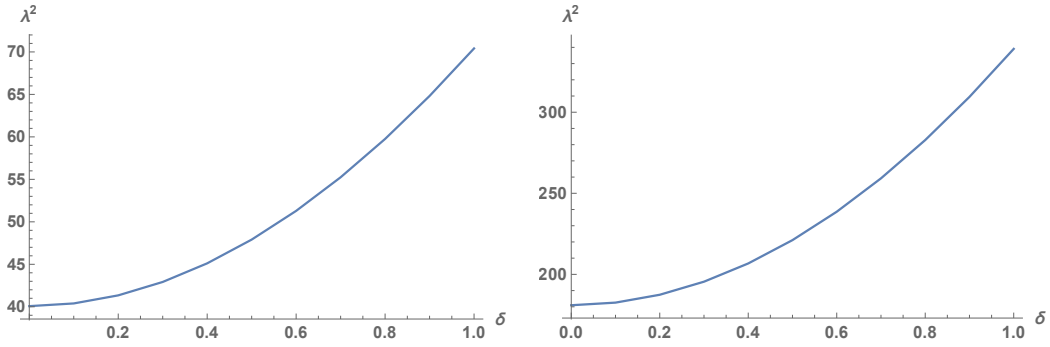

(a) (b)

Figure 4.1: Critical dynamic pressure for different values of porosity constants δ for panels: (a) simply-supported ends; (b) clamped ends.

Note that when considering constant $\psi = 2\delta$, the single-term series solution approximation (4.19) matches the exact solution for uniformly-porous panels (4.28), since the higher-order terms in the Liouville-Neumann series reflect the effect of variation in the porosity function $\psi(x)$.

To determine the critical flow velocity at which divergence occurs for uniformly-porous panels, (4.28) is now substituted into the equation of panel motion (4.3). Considering only the static stability under steady aerodynamic forces, reduces the panel motion equation to

$$\frac{d^4 z_a}{dx^4} + \frac{\lambda^2}{2}\left(\frac{f(x)}{1+\delta^2} - \frac{\delta}{\pi(1+\delta)^2}\left(\frac{x}{1-x}\right)^{k(\delta)} \int_0^1 \frac{f(\xi)}{\xi - x}\left(\frac{1-\xi}{\xi}\right)^{k(\delta)} d\xi\right) = 0. \qquad (4.30)$$

Once again, the special case of (4.30) for the non-porous panels, $\delta = 0$, recovers the expression derived by Kornecki *et al.* [39]. Now, a uniformly-porous panel is considered with harmonic motions, such that $z_a(x,t) = X(x)e^{i\omega t}$ and $p(x,t) = P(x)e^{i\omega t}$. By substitution of (4.29) into (4.30), the critical dynamic pressure, λ^2, at which divergence occurs, is obtained for simply-supported and clamped ends, and it is shown in figure 4.1 for different values of porosity constants δ. Increasing the porosity parameter increases

the critical dynamic pressure, which means that divergence instability occurs at higher flow velocities, and the role of porosity is to suppress the onset of instability.

4.3.2 Dynamic instability

In this section, the critical flow speed and frequency at which instability occurs are examined for porous panels with fixed ends. The singular integral equation (4.4) had been solved in chapter 3 for the non-circulatory pressure distribution over a panel with porosity distribution $R(x)$. Accordingly, the non-circulatory fluid forces for a uniformly-porous panel with harmonic motions, such that $z_a(x,t) = X(x)e^{i\omega t}$ and $p(x,t) = P(x)e^{i\omega t}$, is given by

$$P(x) = \frac{O(x)}{1+\delta^2} - \frac{\delta}{\pi(1+\delta^2)}\left(\frac{x}{1-x}\right)^{\frac{1}{\pi}\tan^{-1}\delta} \int_0^1 \frac{O(\xi)}{\xi - x}\left(\frac{1-\xi}{\xi}\right)^{\frac{1}{\pi}\tan^{-1}\delta} d\xi, \quad (4.31)$$

where

$$O(x) = \frac{2}{\lambda^2}\Big(- \lambda^2 \tilde{I}_0(X,x) - i\omega\lambda\sqrt{\mu_m}\tilde{I}_1(X,x) + \mu_m\omega^2\tilde{I}_2(X,x)\Big), \quad (4.32)$$

and

$$\tilde{I}_0(X,x) = \frac{1}{\pi}\fint_0^1 \frac{X'(\xi)}{x-\xi}d\xi, \quad (4.33)$$

$$\tilde{I}_1(X,x) = \frac{1}{\pi}\fint_0^1 \frac{X(\xi)}{x-\xi} + X'(\xi)\ln|x-\xi|d\xi, \quad (4.34)$$

$$\tilde{I}_2(X,x) = \frac{1}{\pi}\fint_0^1 X(\xi)\ln|x-\xi|d\xi. \quad (4.35)$$

These integrals arise in the analysis of non-porous panels, cf. Kornecki *et al.* [39]. Here $P(x)$ is a complex-valued function, and ω is a dimensionless frequency. Now (4.3) for panels with harmonic motions is given by:

$$\frac{d^4X(x)}{dx^4} - \omega^2 X(x) + \frac{\lambda^2}{2} P(x) = 0, \tag{4.36}$$

which can be recast as the following:

$$\frac{d^4X(x)}{dx^4} - \omega^2 X(x) - \lambda^2 I_0(X,x,\delta) - i\omega\lambda\sqrt{\mu_m} I_1(X,x,\delta) + \mu_m \omega^2 I_2(X,x,\delta) = 0, \tag{4.37}$$

with

$$\begin{aligned} I_i(X,x,\delta) &= \frac{\tilde{I}_i(X,x)}{1+\delta^2} - \frac{\delta}{\pi(1+\delta^2)} \left(\frac{x}{1-x}\right)^{\frac{1}{\pi}\tan^{-1}\delta} \\ &\quad \times \fint_0^1 \frac{\tilde{I}_i(X,\xi)}{\xi - x} \left(\frac{1-\xi}{\xi}\right)^{\frac{1}{\pi}\tan^{-1}\delta} d\xi, \qquad i = 0,1,2. \end{aligned} \tag{4.38}$$

Equation (4.37) has a form exactly like (32) in [39], except for the fact that here the integrals I_0, I_1, and I_2 include extra terms involving the porosity effects. Equations (4.33)-(4.35) are recovered when $\delta = 0$. The solution of (4.37) may be expressed by the series

$$X(x) = \sum_n C_n X_n(x), \tag{4.39}$$

where C_n are constants, and $X_n(x)$ are the beam functions [54],

$$X_n(x) = \cosh(\beta_n x) - \cos(\beta_n x) - \alpha_n \Big[\sinh(\beta_n x) - \sin(\beta_n x) \Big], \tag{4.40}$$

that satisfies the boundary conditions and the equation of free lateral vibration of a beam in a vacuum,

$$\frac{d^4 X_n(x)}{dx^4} - \beta_n^4 X_n(x) = 0. \tag{4.41}$$

Substitution of (4.39) into the (4.37) and application of Galerkin's method yield an infinite set of homogeneous algebraic equations for the constants C_n. These equations have a non-trivial solution, provided that the determinant of their coefficient matrix vanishes [39]:

$$\mathrm{Det}\Big[-\omega^2(\delta_{ij} - \mu_m D_{ij}) + i\omega\lambda\sqrt{\mu_m} B_{ij} + \beta_i^4 \delta_{ij} - \lambda^2 A_{ij} \Big] = 0, \tag{4.42}$$

for $i, j = 1, 2, 3, \cdots$. Here δ_{ij} denotes the Kronecker delta, and A, B, and D are square matrices whose elements are defined by

$$A_{ij} = \int_0^1 X_i(x) I_0(X_j, x) dx, \tag{4.43}$$

$$B_{ij} = \int_0^1 X_i(x) I_1(X_j, x) dx, \tag{4.44}$$

$$D_{ij} = \int_0^1 X_i(x) I_2(X_j, x) dx. \tag{4.45}$$

Note that A_{ij} terms are proportional to the steady aerodynamic forces, B_{ij} to the Coriolis forces, and D_{ij} to the virtual mass of the air surrounding the oscillating panel [39].

The characteristic equation for ω (4.42) is now evaluated numerically for given dimensionless flow velocity λ and corresponding frequency ω for vibrating panels with clamped ends. To solve (4.42), the value of mass ratio μ_m is fixed, two terms in (4.39) are retained, and the following constants satisfying (4.40)-(4.41) and the boundary conditions, are considered for the clamped-clamped panel [54]:

$$\begin{aligned} \beta_1 &= 4.7300408, & \beta_2 &= 7.8532046, \\ \alpha_1 &= 0.9825022158, & \alpha_2 &= 1.000777311. \end{aligned}$$

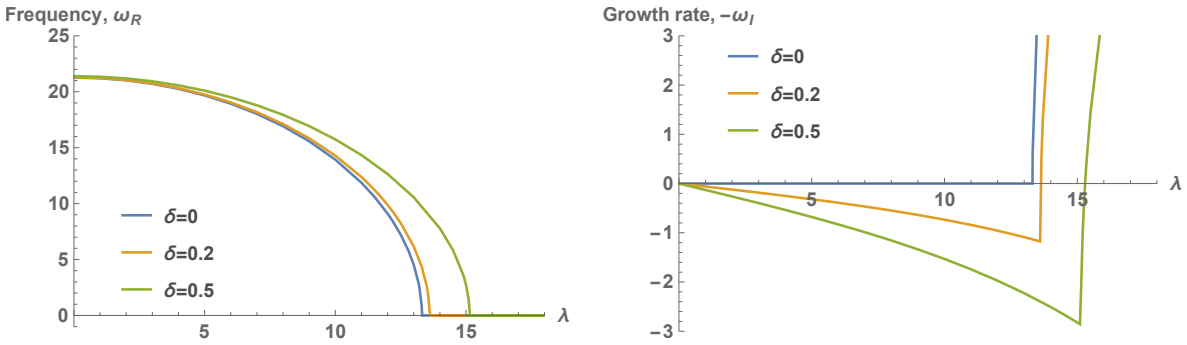

(a) (b)

Figure 4.2: Frequency and growth rate versus the dimensionless flow velocity λ for different values of the porosity parameter δ: (a) frequency, ω_R ; (b) growth rate, $-\omega_I$.

Note that the point of interest is the lowest value of λ for which the motion becomes unstable. Physically, λ must be real and positive, but the frequency ω is a complex number, $\omega = \omega_R + i\omega_I$, where ω_R and $-\omega_I$ indicate the frequency and growth rate, respectively. If the decay rate, $\omega_I > 0$, the motion of the plate is dynamically stable, while it is unstable for $\omega_I < 0$. The aeroelastic stability boundary is defined by the critical flow velocity λ_{cr}, at which one or more roots of (4.42) become neutrally stable, i.e. $\omega_I = 0$. In the solution of (4.42), different values of porosity constants δ will be considered to examine the effects of porosity on the critical flow velocity.

Equation (4.42) has been solved for $\mu_m = 0.25$. Figure 4.2 shows the frequency and growth rate of the root which becomes unstable first, versus λ for non-porous panels with clamped ends, compared against the cases of uniformly-porous panels with values of porosity constants $\delta = 0.2$ and $\delta = 0.5$. This result shows that the first root loses stability by divergence for non-porous as well as porous panels. However, the critical value of λ is larger for porous panels. As it is shown in figure 4.2(b), the non-porous panel is neutrally stable before instability occurs. However, porous panels maintain aeroelastic stability at higher flow speeds before divergence occurs. This observation indicates that porosity acts to damp perturbed or vibrating panels. Note that the mass ratio μ_m does not

affect the value of critical dynamic pressure, since the primary instability is divergence. The independence of the divergence criterion with respect to the mass ratio is obviated by (4.30), since μ_m does not appear in the static aeroelastic equations.

The identification of divergence as the general primary aeroelastic instability mode is now examined rigorously for porous panels. Introducing the parameter $s = i\omega$, (4.42) can be written in the form:

$$a_4 s^4 + \lambda\sqrt{\mu_m} a_3 s^3 + a_2 s^2 + \lambda\sqrt{\mu_m} a_1 s + a_0 = 0, \tag{4.46}$$

where

$$\begin{aligned}
a_4 &= 1 - \mu_m\Big(D_{11} + D_{22}\Big) + \mu_m^2\Big(D_{11}D_{22} - D_{12}D_{21}\Big), \\
a_3 &= -B_{11} - B_{22} + \mu_m\Big(B_{22}D_{11} - B_{21}D_{12} - B_{12}D_{21} + B_{11}D_{22}\Big), \\
a_2 &= \beta_1^4 + \beta_2^4 - A_{11}\lambda^2 - A_{22}\lambda^2 - D_{22}\beta_1^4\mu_m - D_{11}\beta_2^4\mu_m \\
&\quad -\lambda^2\mu_m\Big(B_{12}B_{21} - B_{11}B_{22} - A_{22}D_{11} + A_{21}D_{12} + A_{12}D_{21} - A_{11}D_{22}\Big), \\
a_1 &= -B_{22}\beta_1^4 - B_{11}\beta_2^4 + \lambda^2\Big(A_{22}B_{11} - A_{21}B_{12} - A_{12}B_{21} + A_{11}B_{22}\Big), \\
a_0 &= \beta_1^4\beta_2^4 - A_{22}\beta_1^4\lambda^2 - A_{11}\beta_2^4\lambda^2 - A_{12}A_{21}\lambda^4 + A_{11}A_{22}\lambda^4.
\end{aligned} \tag{4.47}$$

The values of a_i coefficients for the cases considered here are presented in tables C.1-C.3, Appendix C. "The roots s of the characteristic equation (4.46) are examined as λ increases from zero. Real positive roots represent divergence instabilities, while complex roots with positive real parts represent flutter instabilities" [52]. To study the stability of polynomial (4.46), the *Routh-Hurwitz stability criterion* [55] is considered, which provides a necessary and sufficient condition for the stability of a polynomial without solving for the roots directly. Accordingly, satisfying the following conditions, the number of

roots of a quartic polynomial in the closed right half-plane is zero:

$$\begin{cases} a_i > 0, \quad \text{for } i = 0, 1, 2, 3 \\ a_2 a_3 - a_1 a_4 > 0, \\ a_1 a_2 a_3 - a_4 a_1^2 + a_0 a_3^2 > 0, \end{cases} \tag{4.48}$$

without loss of generality, we assume $a_4 > 0$.

Applying the above method to the porous panels presented in tables C.2-C.3, we observe that all conditions in (4.48) are satisfied at $\lambda = 0$, by increasing λ the first changing sign occurs for condition $a_0 > 0$. For the value of critical λ, the imaginary part of the unstable root is zero (one can easily see $s = 0$ is the root), which indicates that the divergent instability occurs before the flutter instability.

It should be noted that one can always find a numerical approximation of roots, which may be computationally expensive, depending on the size of your problem. However, according to this method, aeroelastic instability can be simply established based on the sign of six terms.

4.4 Chapter summary

The non-circulatory fluid forces on an oscillating porous panel are applied to aeroelastic stability predictions for porous panels or liners, fixed at both ends. The effect of porosity has been investigated, and it is shown that a porous panel with fixed ends loses its stability by divergence, which is in agreement with the classical result for non-porous panels. Therefore, porosity does not change the type of primary aeroelastic instability.

However, divergence instability occurs in higher flow speeds for porous panels compare to the non-porous ones, this critical flow speed increases as the porosity parameter δ

increases. These observations indicate that porosity damps and stabilizes elastic panels in an external flow.

Chapter 5

Acoustic emission from porous panels

The acoustic far-field pressure is determined for finite-chord panels with uniform porosity in a single-sided uniform flow. The free space Green's function for the two-dimensional Helmholtz equation propagates into the acoustic field the unsteady non-circulatory forces on the panel, which are known in closed form from established analysis. Results from this chapter identify the sensitivity of the noise level and directivity from vibrating panels to changes in Mach number, reduced frequency, and the magnitude of a Darcy-type porosity parameter.

5.1 Introduction

The acoustic pressure field for vibrating panels may be computed from the Rayleigh integral [49], which is a two-dimensional convolution of the vibrational velocity and the Green's function. These vibrating panels are typically not porous, but porosity effects have been implemented in aerodynamic noise scenarios as a passive means to suppress low-frequency noise generation [8, 56]. A large body of research has recently emerged to predict the impact of the edge condition on the trailing edge turbulence scattering mecha-

nism [7–10, 56–61]. Howe [58] examined the scattering of turbulent noise sources from a semi-infinite rigid plane with porosity at the trailing edge section. Porosity and elasticity are combined to study the transmission of incident sound through an infinite poroelastic plate [7], and this model has been employed by Jaworski and Peake [8] to investigate the scattering of turbulent noise sources from a poroelastic half-plane. Accordingly, trailing-edge porosity and elasticity can be tuned in a scaling sense to eliminate the predominant scattering mechanism of trailing edge noise.

The present chapter investigates theoretically whether or not porosity can also be an effective means of structural noise suppression for one-dimensional panels. Data measured by Fahy [50] for vibrating panels indicates that for high-porosity panels the sound radiation efficiency is reduced by a factor of at least five. In that study, the accompanying theoretical results for non-perforated panels are not applicable to perforated ones, and the present analysis seeks to fill this knowledge gap. The analysis proceeds by using the Green's function method to propagate known surface pressures into the acoustic field. Accordingly, the values of pressure in the far field can be obtained based on the value of the pressure on the plate at a given frequency [62]. Using the Green's function method, Atassi *et al.* [36] have obtained an exact expression for the far-field acoustic pressure from the interaction of impinging unsteady vortical disturbances on a thin airfoil in subsonic flow, where it was shown that the acoustic pressure pattern strongly depends on the value of the reduced frequency and the mean flow Mach number.

In this chapter, the free space Green's function for the two-dimensional Helmholtz equation is combined with the non-circulatory pressure distribution determined in chapter 3 to predict the acoustic far-field pressure of a vibrating porous panel. Results from this study seek to identify the effects of varying the magnitude of a Darcy-type porosity condition, the reduced frequency, and the mean flow Mach number on the acoustic

emission of vibrating panels.

5.2 Mathematical model

Consider a thin panel undergoing prescribed unsteady motions in a two-dimensional steady, incompressible flow. For non-circulatory forces, it is sufficient to consider the baffled panel with single-sided flow illustrated in figure 3.1, as neither a vortex sheet nor the Kutta condition are imposed here. Based upon the work of Patrik *et al.* [62], the far-field pressure can be determined by knowing the non-circulatory pressure distribution on the boundary and the free space Green's function for the two-dimensional Helmholtz equation. The means of determining the free space Green's function critical to the acoustic problem are outlined in the following sections.

5.2.1 Acoustics of a porous panel

This section aims to calculate the acoustics emission from a porous deforming panel in subsonic flow. The radiated sound is the far-field solution to the unsteady aerodynamic problem, which is evaluated by Kirchhoff method [36], using the Green's function approach. In the upper half plane above the panel, the governing equation for the acoustic pressure is shown to be the 2D convective wave equation [62]:

$$\left[M_\infty^2 \left(\frac{\partial}{\partial t} + \frac{\partial}{\partial x_1}\right)^2 - \nabla^2\right] p(\mathbf{x}, t) = 0, \tag{5.1}$$

where c is the speed of sound and M_∞ defines the Mach number. For the observation and source points $\mathbf{x} = (x_1, x_2)$ and $\mathbf{y} = (y_1, y_2)$, a transformation to the Prandtl-Glauert plane ($\tilde{x}_1 = x_1$, $\tilde{x}_2 = \beta_\infty x_2$) and transform $P = p(\mathbf{x}, t) e^{-i(\omega t + M_\infty K x_1)}$ following Reissner [63]

and Graham [64] results in

$$
\begin{aligned}
- \quad & \Big(1 - M_\infty^2\Big)\tilde{\nabla}^2 P + 2iM_\infty\Big(\omega M_\infty + KM_\infty^2 - K\Big)\frac{\partial P}{\partial x_1} \\
& + M_\infty^2\Big(K^2 - 2M_\infty K\omega - \omega^2 - M_\infty^2 K^2\Big)P = 0,
\end{aligned} \tag{5.2}
$$

where ω is a dimensionless frequency $\omega = \omega_0 l/U$, for dimensional ω_0. By choosing

$$
K = \frac{\omega M_\infty}{{\beta_\infty}^2}, \tag{5.3}
$$

where $\beta_\infty^2 = 1 - M_\infty^2$, the coefficient of $\partial P/\partial x_1$ vanishes, and the convective wave equation is reduced to a Helmholtz equation for P:

$$
\Big(\tilde{\nabla}^2 + K^2\Big)P = 0, \tag{5.4}
$$

Green's theorem is now employed to evaluate the values of P in the acoustic far field, based on the value of the pressure on the plate at a given frequency [62]:

$$
P(\tilde{\mathbf{x}}) = \frac{1}{2\pi}\int_s \Big[P(\tilde{\mathbf{y}})\frac{\partial G(\tilde{\mathbf{y}}|\tilde{\mathbf{x}})}{\partial n} - G(\tilde{\mathbf{y}}|\tilde{\mathbf{x}})\frac{\partial P(\tilde{\mathbf{y}})}{\partial n}\Big]ds. \tag{5.5}
$$

Here $\tilde{\mathbf{x}}$ and $\tilde{\mathbf{y}}$ are the observation and source points, respectively, in the Prandtl-Glauert plane. The Kirchhoff surface s encloses all the acoustic singularities and the solid boundaries. In this case, the Kirchhoff surface is simply a curve in two-dimensional problems and is chosen to be a circle in the Prandtl-Glauert plane. In (5.5), G denotes the free space Green's function, which is defined as satisfying the two-dimensional Helmholtz equation:

$$
\Big(\tilde{\nabla}_{\tilde{\mathbf{y}}}^2 + K^2\Big)G(\tilde{\mathbf{y}}|\tilde{\mathbf{x}}) = -2\pi\boldsymbol{\delta}(\tilde{\mathbf{y}} - \tilde{\mathbf{x}}), \tag{5.6}
$$

where $\boldsymbol{\delta}$ defines the Dirac delta function. The solution to (5.6) is given by:

$$G(\tilde{\mathbf{y}}|\tilde{\mathbf{x}}) = -i\frac{\pi}{2}H_0^{(2)}\Big(K|\tilde{\mathbf{y}} - \tilde{\mathbf{x}}|\Big), \tag{5.7}$$

where $H_0^{(2)}$ is the Hankel function of the second kind. Note that the choice of Hankel function is time dependent, and it is chosen such that all acoustic waves are outgoing.

To find the acoustic far-field pressure from (5.5), $\partial G/\partial n$ and $\partial P/\partial n$ are evaluated on the panel surface. Using the free space Green's function (5.7), it can be established that:

$$\frac{\partial G(\tilde{\mathbf{y}}|\tilde{\mathbf{x}})}{\partial \tilde{y}_2}\Big|_{\tilde{y}_2=0} = -\frac{i\pi K\beta_\infty x_2}{2}\frac{H_1^{(2)}\Big(K|\tilde{\mathbf{y}} - \tilde{\mathbf{x}}|\Big)}{|\tilde{\mathbf{y}} - \tilde{\mathbf{x}}|}. \tag{5.8}$$

Also, $\partial P/\partial n$ can be evaluated using the linearized Euler equation for incompressible flows:

$$\begin{aligned}
\frac{\partial P(\tilde{\mathbf{y}})}{\partial \tilde{y}_2}\Big|_{\tilde{y}_2=0} &= \frac{\partial p(\tilde{\mathbf{y}}, t)}{\partial \tilde{y}_2}\Big|_{\tilde{y}_2=0} e^{-i(\omega t + M_\infty K y_1)} \\
&= \frac{-2}{\beta_\infty}\left(\frac{\partial^2 \phi}{\partial y_2 \partial t} + \frac{\partial^2 \phi}{\partial y_2 \partial y_1}\right) e^{-i(\omega t + M_\infty K y_1)} \\
&= \frac{-2}{\beta_\infty}\Big(\frac{\partial w(y_1, t)}{\partial t} + \frac{\partial w(y_1, t)}{\partial y_1}\Big) e^{-i(\omega t + M_\infty K y_1)},
\end{aligned} \tag{5.9}$$

where $w(y_1, t) = \partial\phi/\partial y_2|_{y_2=0}$ is the perturbation flow velocity on the panel surface and given by [19]

$$w(y_1, t) = w_s + \frac{\partial z_a}{\partial y_1} + \frac{\partial z_a}{\partial t}. \tag{5.10}$$

Here w_s defines the seepage velocity. For an airfoil with a Darcy-type porosity distribution, the local flow rate is linearly proportional to the porosity and dimensionless pressure

distribution [19, 25]:

$$w_s = -\frac{1}{2}\rho UCR(y_1)p(y_1,t). \tag{5.11}$$

In the next section, the acoustic far-field pressure is studied numerically for uniformly-porous panels with simply-supported ends.

5.3 Uniformly-porous panels with simply-supported ends

This section provides numerical solution for the acoustic emission from the special case of uniformly-porous panels, $R(x) = 1$, with simply-supported ends. For uniformly-porous panels with harmonic motions, such that $z_a(x,t) = X(x)e^{i\omega t}$ and $p(x,t) = \bar{P}(x)e^{i\omega t}$, where $\bar{P}(x)$ is a complex-valued function, the non-circulatory fluid forces had been expressed in chapter 3 and is given by

$$\bar{P}(x) = \frac{O(x)}{1+\delta^2} - \frac{\delta}{\pi(1+\delta^2)}\left(\frac{x}{1-x}\right)^{\frac{1}{\pi}\tan^{-1}\delta} \int_0^1 \frac{O(\xi)}{\xi - x}\left(\frac{1-\xi}{\xi}\right)^{\frac{1}{\pi}\tan^{-1}\delta} d\xi, \tag{5.12}$$

where

$$\begin{aligned} O(x) &= \frac{2}{\pi}\fint_0^1 \frac{X'(\xi) + i\omega X(\xi)}{\xi - x} d\xi \\ &\quad -\frac{2i\omega}{\pi}\int_0^1 [X'(\xi) + i\omega X(\xi)] \ln|x-\xi| d\xi. \end{aligned} \tag{5.13}$$

Considering the simply-supported boundary condition $X(x) = \epsilon \sin(\pi x)$, $\epsilon = 0.01$, (5.9) can be recast in the following form:

$$\begin{aligned} \frac{\partial P(\tilde{y}_2)}{\partial \tilde{y}_2}\Big|_{\tilde{y}_2=0} = \quad & \frac{1}{\beta_\infty}\Big[2\epsilon(\pi^2+\omega^2)\sin(\pi y_1) - 4i\epsilon\pi\omega\cos(\pi y_1) \\ & +\delta\left(\frac{\partial \bar{P}(y_1)}{\partial y_1} + i\omega\bar{P}(y_1)\right)\Big] e^{-iM_\infty K y_1}, \end{aligned} \tag{5.14}$$

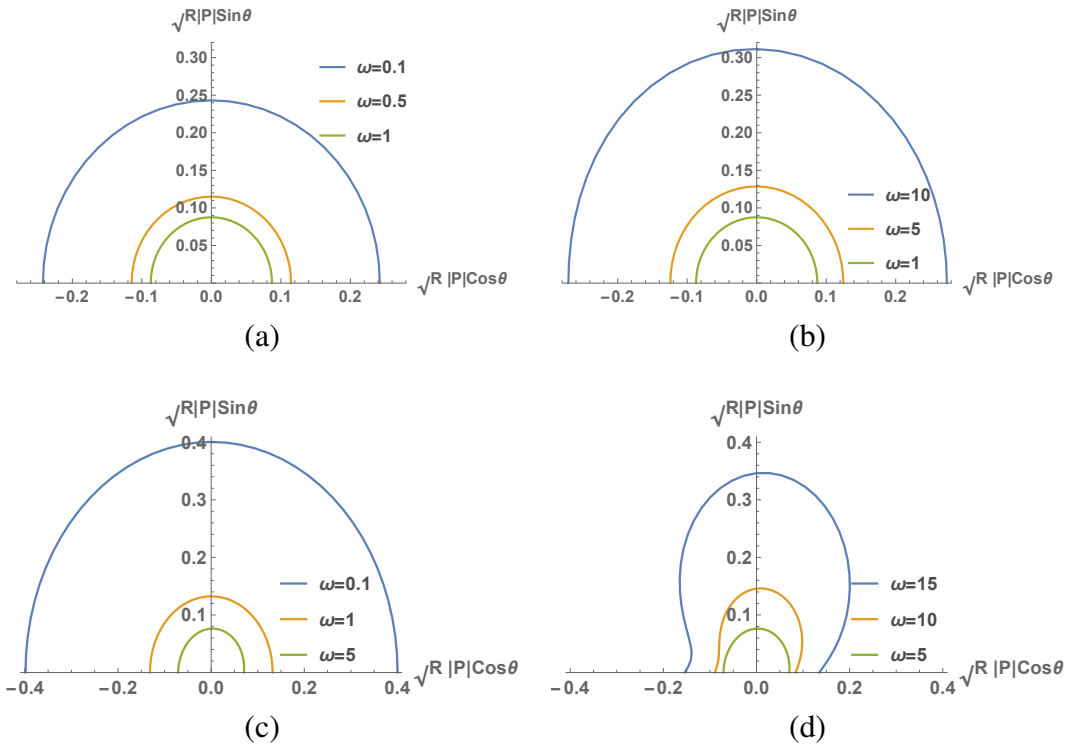

Figure 5.1: Acoustic emission at $M = 0.1$ for different values of frequency: (a)-(b) from a non-porous vibrating panel, (c)-(d) from a porous vibrating panel with $\delta = 0.5$.

where $\bar{P}$ defines the pressure distribution on the panel and given by (5.12). Implementation of the pressure distribution on the plate and solving the aforementioned integrals given by (5.8) and (5.14) lead to the pressure evaluation at any point in the field of interest (5.5). Note that the theory presented in chapter 3 is derived for incompressible flows, therefore in the present work acoustic pressures are evaluated for background mean flows with $M \lesssim 0.3$ for consistency.

Figure 5.1 shows the amplitude of acoustic pressure produced by a non-porous and a porous panel for $M = 0.1$ and $\delta = 0.5$ at different values of reduced frequency. The panel considered in this problem is exposed to a single-sided flow and therefore propagates the acoustic pressure into the field similar to a monopole sound source. Figure 5.1(a) indicates that the far-field pressure produced by a non-porous panel is symmetric for a

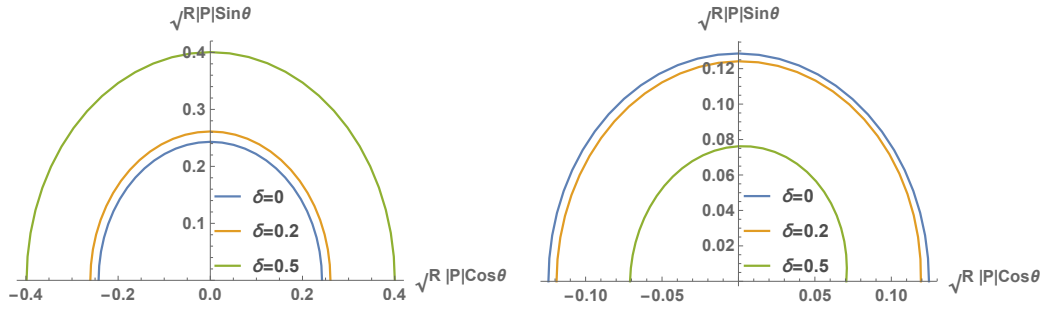

Figure 5.2: Comparison between acoustic emission from porous and non-porous panels at $M = 0.1$ for: (a) $\omega = 0.1$; (b) $\omega = 5$.

fixed Mach number. Moreover, at low frequencies, the amplitude of the produced sound decreases by increasing ω, however, for frequencies larger than a critical value ω^*, the sound produced by structural vibration increases for larger values of frequencies. Similar behavior is observed in figure 5.1(b) for vibrating porous panels with $\delta = 0.5$; however, porosity breaks the symmetry for large ω and increases the value of ω^*.

A comparison has been made between the acoustic emission from porous and non-porous panels in figure 5.2. As illustrated in figure 5.2(b), for a fixed Mach number $M = 0.1$, the acoustic pressure emission from non-porous panel decreases by introducing porosity at frequency $\omega = 5$. However, figure 5.2(a) indicates that porous panels produce larger sound pressure at lower reduced frequency $\omega = 0.1$.

Figures 5.3-5.5 investigate the effect of Mach number in the far-field acoustic emission for non-porous and porous panels. At a constant reduced frequency $\omega = 5$, by increasing the Mach number, larger values of porosity parameter δ are needed to reduce the sound generated from vibrating panels in all directions. The result of this study indicates that even at high frequencies, introduction of porosity does not always reduces the sound pressure.

5.4 Chapter summary

This chapter determines the acoustic far-field pressure for finite-chord porous panels . The free space Green's function for the two-dimensional Helmholtz equation propagates into the acoustic field of the unsteady non-circulatory forces on the panel, which are known in closed form from established analysis. The amplitude of the sound produced by panels with different porosity is compared for different values of porosity parameters δ and frequencies. Results from this study indicate that, at low Mach numbers, increasing the magnitude of a Darcy-type porosity parameter leads to a reduction in the acoustic emission from a vibrating panel at high frequencies, while the introduction of porosity does not reduce the sound pressure for lower frequencies and larger Mach numbers.

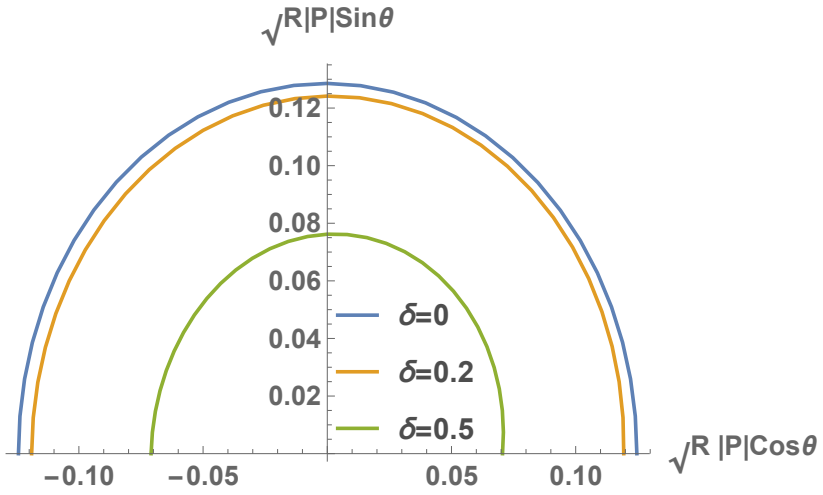

Figure 5.3: Comparison between the acoustic emission from non-porous and porous panels with $\delta = 0.2$ and $\delta = 0.5$ at $\omega = 5$ and $M = 0.1$.

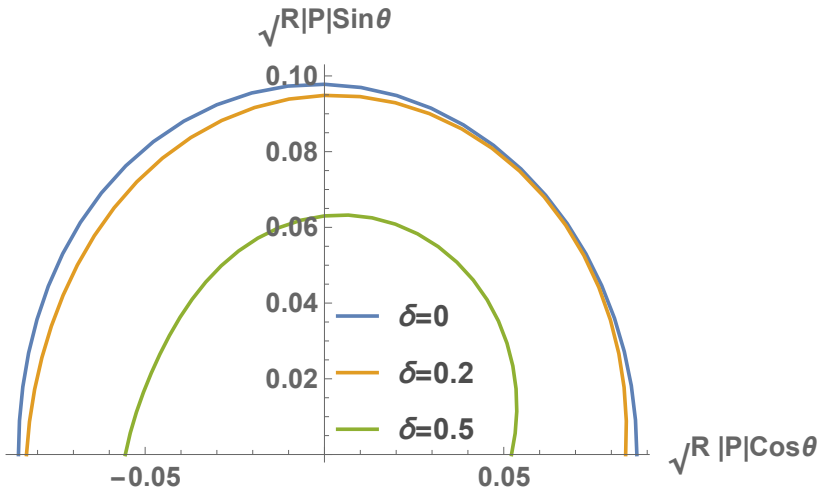

Figure 5.4: Comparison between the acoustic emission from non-porous and porous panels with $\delta = 0.2$ and $\delta = 0.5$ at $\omega = 5$ and $M = 0.2$.

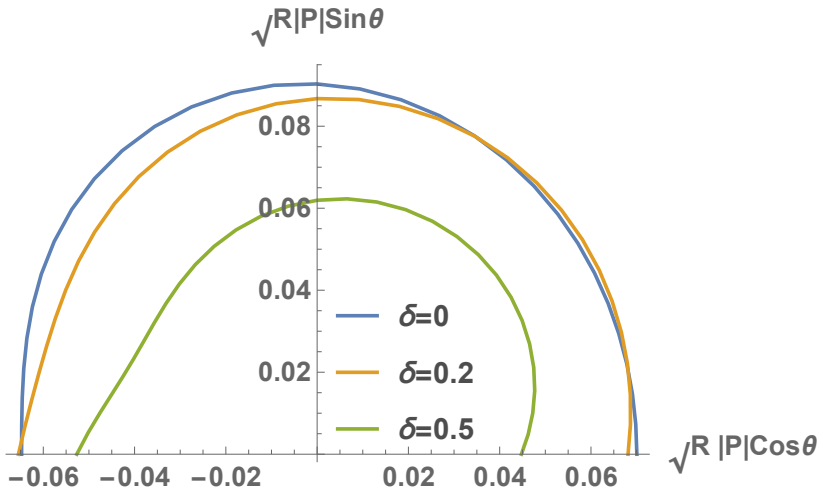

Figure 5.5: Comparison between the acoustic emission from non-porous and porous panels with $\delta = 0.2$ and $\delta = 0.5$ at $\omega = 5$ and $M = 0.3$.

Chapter 6

Conclusions and Future Directions

This dissertation determines the aerodynamics, structural acoustics, and aeroelastic stability of porous airfoils and panels. An exact solution is determined for the pressure distribution over an airfoil in a steady incompressible flow with a prescribed Hölder-continuous porosity distribution. Aerodynamic loads coefficients, lift, moment coefficients, and seepage drag can be obtained in closed form for the special case of a uniformly-porous airfoil. Previous analytical results for partially-porous airfoils are recovered by the new general solution for certain limiting cases of piecewise-continuous and differentiable porosity distributions, which further verify the present results. A comparison of the lift prediction for a porous SD7003 airfoil against available experimental data indicates good agreement for sufficiently small values of the nondimensional porosity parameter that depends on the flow and porosity of the airfoil material. For large values of the porosity parameter, the model predicts negative lift, a phenomenon due to the camber of porous airfoils and not the angle of attack.

From linearized aerodynamic theory, a Fredholm integral equation is derived and solved analytically as a Liouville-Neumann series for the non-circulatory pressure distribution on an oscillating porous panel or airfoil in a uniform incompressible flow. The fun-

damental integral equation results from the application of a Darcy-type porosity boundary condition that has a Hölder-continuous spatial distribution along the chord. The pressure distribution is determined explicitly for the case of a single frequency, which can be used to determine the pressure distribution resulting from arbitrary panel deformations with a Fourier series in time. The non-circulatory pressure distributions for vibrating panels on simple or clamped supports with either uniform or variable chordwise porosity distributions are presented and compared. Porosity breaks the well-known left-right symmetry of the non-porous pressure distribution, reduces the pressure peak, and shifts the peak location towards the trailing edge for increasing values of the porosity parameter δ. The magnitude and aftward shift of the peak is affected by the prescribed chordwise porosity gradient. The non-circulatory pressure distribution over the clamped panel is regular at the leading edge for all time instants considered, but a simply-supported panel with sinusoidal displacement generates a pressure singularity at the leading edge. At the leading edge, porous panels retain the singular or regular behavior of their non-porous counterpart. A singular behavior is always observed at the trailing edge for porous panels, with the exception of cases where the porosity vanishes at the trailing edge. The choice of a porosity function that vanishes at the trailing edge recovers the regular behavior of the pressure field observed for non-porous panels.

The non-circulatory fluid forces on an oscillating porous panel are applied to aeroelastic stability predictions for porous panels or liners, fixed at both ends. It is shown that a porous panel with both ends fixed loses its stability by divergence, which is in agreement with the classical result for non-porous panels. Therefore, porosity does not change the type of primary instability. However, divergence instability occurs in higher flow velocities for porous panels compare to non-porous ones. These observations indicate that porosity stabilizes elastic panels in an external flow.

The unsteady non-circulatory forces on the panel are coupled with the free space Green's function for the two-dimensional Helmholtz equation to determine the acoustic far-field pressure for finite-chord porous panels vibrating in a single-sided flow. It is shown that the sound pressure produced by a uniformly-porous airfoil relative to its non-porous counterpart depends on the reduced frequency, Mach number, and the dimensionless porosity parameter. At low Mach numbers, increasing the magnitude of a Darcy-type porosity parameter leads to a reduction in the acoustic emission from a vibrating panel at high frequencies, while the introduction of porosity does not reduce the produced sound pressure at lower frequencies. Furthermore, it is demonstrated that, even at high frequencies, porosity does not always reduce the sound pressure; by increasing the Mach number, larger values of porosity parameter are needed to reduce the sound generated from vibrating panels in all directions.

This dissertation is concluded with a few future works and open problems. The work presented in this dissertation was focused on the stationary and non-circulatory aerodynamic loads on porous panels. A promising future research direction is to investigate the circulatory effects to form a complete unsteady aerodynamic theory of porous airfoils. Moreover, this study could be extended to include an optimization analysis based on the trade-off between the acoustical advantage and aerodynamic penalty of porous bodies.

Appendix A

SD7003 camber line and thickness distributions

The slope of the mean surface of the wing, dz/dx, and thickness distribution, $d(x)$, are based on the SD7003 airfoil coordinates given in [30] and are approximated by the following expressions:

$$\begin{aligned}\frac{dz}{dx} &= 0.0456479 + 0.00359184(1+x)^{-1/2} - 0.179623(1+x) \\ &\quad +0.287101(1+x)^2 - 0.270092(1+x)^3 + 0.134608(1+x)^4 \\ &\quad -0.0270882(1+x)^5, \end{aligned} \tag{A.1}$$

$$\begin{aligned}d(x) &= -0.00256 + 0.21524(1+x)^{1/2} - 0.09707(1+x) \\ &\quad -0.057069(1+x)^2 - 0.059067(1+x)^3 + 0.131062(1+x)^4 \\ &\quad -0.0790595(1+x)^5 + 0.0160312(1+x)^6. \end{aligned} \tag{A.2}$$

Appendix B

Verification of generalized steady aerodynamic solution

The general solution (2.22) for Hölder-continuous porosity distributions is here shown to recover the theoretical results presented by Iosilevskii [1] for parabolic, uniform-porosity airfoils. A closed form expression is obtained for the pressure distribution over a uniformly-porous airfoil with parabolic camber line, for which the camber-to-chord ratio is $\beta/4$, and

$$\frac{dz}{dx} = -\alpha - \beta x. \tag{B.1}$$

Substitution of (B.1) into (2.24) leads to the closed form expression for the pressure distribution over a uniformly-porous airfoil with a parabolic camber line. Following the evaluation of the Cauchy principal value integral,

$$\begin{aligned} \fint_{-1}^{1} \frac{(-\alpha-\beta x)}{x-t}\Big(\frac{1+t}{1-t}\Big)^{k(2\delta)} dt &= \pi\sqrt{1+4\delta^2}(\alpha+\beta x+2k(2\delta)\beta) \\ &\quad -\pi\psi(\alpha+\beta x)\Big(\frac{1+x}{1-x}\Big)^{k(2\delta)}, \end{aligned}$$

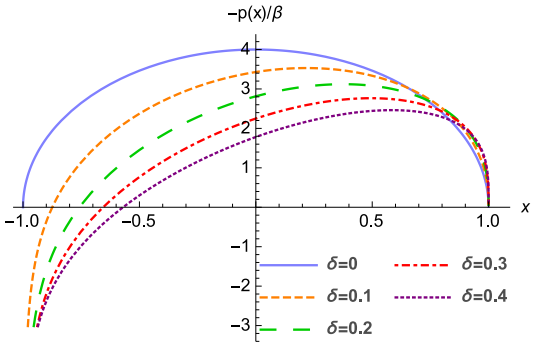

Figure B.1: Normalized pressure distribution, $-p(x)/\beta$, of a uniformly-porous cambered airfoil at zero angle of attack ($\alpha = 0$) for different porosity constants δ.

the pressure distribution is:

$$p(x) = \frac{-4}{\sqrt{1+4\delta^2}}\Big(\alpha + \beta(x + 2k(2\delta))\Big)\Big(\frac{1-x}{1+x}\Big)^{k(2\delta)}. \tag{B.2}$$

This pressure distribution for the uniformly-porous airfoil is the same as the result of Iosilevskii, equation (40) in [1], for an airfoil with piecewise-constant porosity using an independent asymptotic analysis approach. According to (B.2), increasing the porosity parameter decreases the pressure distribution over the uniform-porosity airfoil, as illustrated in figure B.1. For $\delta \gg 1$, the pressure distribution becomes linearly proportional to x with slope $-2\beta/\delta$,

$$p(x) \sim \frac{-2(\alpha + \beta x)}{\delta}, \tag{B.3}$$

when sufficiently far from the leading and trailing edges. For uniformly-porous airfoil with a parabolic camber line, the lift, pitching moment, and seepage drag can be predicted from the pressure distribution provided by (B.2). The sectional lift coefficient is directly calculated by

$$c_L = -\frac{1}{2}\int_{-1}^{1} p(x)dx = 4k(2\delta)\pi\alpha + 4k(2\delta)^2\pi\beta. \tag{B.4}$$

Note that the obtained lift coefficient for a uniformly porous airfoil with a parabolic camber line in (B.4) recovers equation (42) in [1] as $a \to -1$. The agreement of aerodynamic loads in this limit suggests that the universal constant for the suction force acting on an impermeable leading edge (see Appendix E of [1]) is unaffected by the imposition of porosity at the leading edge.

Appendix C

Coefficients for dynamic instability prediction of porous panels

The values of a_i coefficients given by (4.47) are presented in the following for different values of porosity parameter δ.

a_i	$\delta = 0$
a_0	$1.90391 \times 10^6 - 13890.5\lambda^2 + 17.7704\lambda^4$
a_1	0
a_2	$4304.1 - 9.11693\lambda^2 + 1719.62\mu - 1.10206\mu\lambda^2$
a_3	0
a_4	$1 + 0.624449\mu + 0.0845411\mu^2$

Table C.1: a_i coefficients for non-porous panels.

a_i	$\delta = 0.2$
a_0	$1.90391 \times 10^6 - 13397.2\lambda^2 + 16.9317\lambda^4$
a_1	$1192.01 - 0.747522\lambda^2$
a_2	$4304.1 - 8.77767\lambda^2 + 1679.51\mu - 1.00571\lambda^2\mu$
a_3	$0.636395 + 0.0955292\mu$
a_4	$1 + 0.607689\mu + 0.0811426\mu^2$

Table C.2: a_i coefficients for porous panels with $\delta = 0.2$.

a_i	$\delta = 0.5$
a_0	$1.90391 \times 10^6 - 11302.1\lambda^2 + 13.5212\lambda^4$
a_1	$2534.13 - 1.35312\lambda^2$
a_2	$4304.1 - 7.34557\lambda^2 + 1504.25\mu - 0.635413\lambda^2\mu$
a_3	$1.34087 + 0.18462\mu$
a_4	$1 + 0.535261\mu + 0.0669656\mu^2$

Table C.3: a_i coefficients for porous panels with $\delta = 0.5$.

Bibliography

[1] G. Iosilevskii, "Aerodynamics of permeable membrane wings. part 2: Seepage drag," *European Journal of Mechanics B/Fluids*, vol. 39, pp. 32–41, 2013.

[2] ——, "Aerodynamics of permeable membrane wings," *European Journal of Mechanics B/Fluids*, vol. 30, pp. 534–542, 2011.

[3] T. F. Brooks, D. S. Pope, and M. A. Marcolini, "Airfoil self-noise and prediction," *NASA Technical Reports Server*, vol. 1218, 1989.

[4] R. E. Hayden, "Reduction of noise from airfoils and propulsive lift systems using variable impedance systems," in *3*rd *AIAA Aeroacoustics Conference, Palo Alto, CA*. Paper AIAA-1976-500, July 1976.

[5] J. E. Ffowcs Williams and L. H. Hall, "Aerodynamic sound generation by turbulent flow in the vicinity of a scattering half plane," *Journal of Fluid Mechanics*, vol. 40, pp. 657–670, 1970.

[6] M. S. Howe, "Structural and acoustic noise produced by turbulent flow over an elastic trailing edge," *Proceedings of the Royal Society of London A*, vol. 442, no. 1916, pp. 533–554, 1993.

[7] ——, *Acoustics of fluid-structure interactions*. Cambridge University Press, 1998.

[8] J. W. Jaworski and N. Peake, "Aerodynamic noise from a poroelastic edge with implications for the silent flight of owls," *Journal of Fluid Mechanics*, vol. 723, pp. 456–479, 2013.

[9] T. Geyer, E. Sarradj, and C. Fritzsche, "Measurement of the noise generation at the trailing edge of porous airfoils," *Experiments in Fluids*, vol. 48, no. 2, pp. 291–308, 2010.

[10] T. Geyer and E. Sarradj, "Trailing edge noise of partially porous airfoils," in *20*th *AIAA/CEAS Aeroacoustics Conference, Atlanta, GA*. Paper AIAA-2014-3039, June 2014.

[11] D. G. Crighton and F. G. Leppington, "Scattering of aerodynamic noise by a semi-infinite compliant plate," *Journal of Fluid Mechanics*, vol. 43, pp. 721–736, 2006.

[12] J. E. Ffowcs Williams, "The acoustics of turbulence near sound-absorbent liners," *Journal of Fluid Mechanics*, vol. 51, no. 4, pp. 737–749, 1972.

[13] L. J. Ayton, "Acoustic scattering by a finite rigid plate with a poroelastic extension," *Journal of Fluid Mechanics*, vol. 791, pp. 414–438, 2016.

[14] A. V. G. Cavalieri, W. R. Wolf, and J. W. Jaworski, "Numerical solution of acoustic scattering by finite perforated elastic plates," *Proceedings of the Royal Society of London A*, vol. 472, no. 2188, 2016, 20150767.

[15] M. Weidenfeld and A. Manela, "On the attenuating effect of permeability on the low frequency sound of an airfoil," *Journal of Sound and Vibration*, vol. 375, pp. 275–288, 2016.

[16] L. C. Woods, "Generalized aerofoil theory," *Proceedings of the Royal Society A*, vol. 238, no. 1214, 1957.

[17] Y. Bae and Y. J. Moon, "Effect of passive porous surface on the trailing-edge noise," *Physics of Fluids*, vol. 23, no. 12, 2011, 126101.

[18] B. Y. Zhou, N. R. Gauger, S. R. Koh, M. Meinke, and W. Schröder, "On the adjoint-based control of trailing-edge turbulence and noise minimization via porous material," in *21st AIAA/CEAS Aeroacoustic Conference, Dallas, TX*. Paper AIAA-2015-2530, 2015.

[19] R. Hajian and J. W. Jaworski, "The steady aerodynamics of aerofoils with porosity gradients," *Proceedings of the Royal Society A*, vol. 473, no. 2205, 2017, 20170266.

[20] H. Ashley and M. Landahl, *Aerodynamics of wings and bodies*. Addison-Wesley Publishing Company, Inc, 1965.

[21] I. H. Abbott and A. E. V. Doenhoff, *Theory of wing sections*. Dover Publication, Inc, 1958.

[22] R. Hajian and J. W. Jaworski, "Steady aerodynamics of thick and cambered airfoils with porosity gradients," in *54th AIAA Aerospace Sciences Meeting, San Diego, CA*. Paper AIAA-2016-0855, January 2016.

[23] R. L. Bisplinghoff, H. Ashley, and R. L. Halfman, *Aeroelasticity*. New York: Dover Publications, 1996.

[24] M. Van Dyke, *Perturbation methods in fluid mechanics*. Parabolic Press, 1975.

[25] I. K. Lifanov, A. F. Matveev, and I. M. Molyakov, "Flow around permeable and thick airfoils and numerical solution of singular integral equations," *Russian Journal of Numerical Analysis and Mathematical Modelling*, vol. 7, no. 2, pp. 109–144, 2009.

[26] N. I. Muskhelishvili, *Singular integral equations*. Gröningen: Noordhoff, 1953.

[27] M. L. Dow and D. Elliott, "The numerical solution of singular integral equations over $(-1, 1)$," *SIAM Journal on Numerical Analysis*, vol. 16, no. 1, pp. 115–134, 1979.

[28] F. D. Gakhov, *Boundary value problems*. New York: Dover Publications, 1990.

[29] R. Hajian and J. W. Jaworski, "The steady aerodynamics of quiet airfoils with porosity gradients," in *45th AIAA Fluid Dynamics Conference, Dallas, TX*. Paper AIAA-2015-2304, June 2015.

[30] "UIUC airfoils coordinates database," ⟨http://m-selig.ae.illinois.edu/ads/coord_database.html⟩.

[31] S. Ergun, "Fluid flow through packed columns," *Chemical Engineering Progress*, vol. 48, pp. 89–94, 1952.

[32] T. Theodorsen, "General theory of aerodynamic instability and the mechanism of flutter," *NACA Report-496*, 1949.

[33] J. W. Jaworski, "Thrust and aerodynamic forces from an oscillating leading edge flap," *AIAA Journal*, vol. 50, no. 12, pp. 2928–2931, 2012.

[34] M. Gaunaa, "Unsteady two-dimensional potential-flow model for thin variable geometry airfoils," *Wind Energy*, vol. 13, pp. 167–192, 2010.

[35] W. R. Sears, "Some aspects of non-stationary airfoil theory and its practical application," *AIAA Journal*, vol. 8, no. 3, pp. 104–108, 1941.

[36] H. M. Atassi, M. Dusey, and C. M. Davis, "Acoustic radiation from a thin airfoil in nonuniform subsonic flows," *AIAA Journal*, vol. 31, no. 1, pp. 12–19, 1993.

[37] T. Ishii, "Aeroelastic instabilities of simply supported panels in subsonic flow," in *AIAA Aircraft Design and Technology Meeting, Los Angeles, CA*. Paper AIAA-65-772, 1965.

[38] T. Gislason, "Experimental investigation of panel divergence at subsonic speeds," *AIAA Journal*, vol. 9, no. 11, pp. 2252–2258, 1971.

[39] A. Kornecki, E. H. Dowell, and J. O'Brien, "On the aeroelastic instability of two-dimensional panels in uniform incompressible flow," *Journal of Sound and Vibration*, vol. 47, no. 2, pp. 163–178, 1976.

[40] E. H. Dowell, *Aeroelasticity of plates and shells*. Noordhoff, 1974.

[41] J. M. Hedgepeth, "Flutter of rectangular simply supported panels at high supersonic speeds," *Journal of the Aeronautical Sciences*, vol. 24, no. 8, pp. 563–573, 1957.

[42] S. K. Datta and W. G. Gottenberg, "Instability of an elastic strip hanging in an airstream," *Journal of Applied Mechanics*, vol. 42, pp. 195–198, 1975.

[43] M. A. Biot, "The divergence of supersonic wings including chordwise bending," *Journal of the Aeronautical Sciences*, vol. 23, no. 3, pp. 237–252, 1956.

[44] R. Hajian and J. W. Jaworski, "Non-circulatory fluid forces on panels and airfoils with porosity gradients," in *8th AIAA Theoretical Fluid Mechanics Conference, Denver, CO*. Paper AIAA-2017-4339, June 2017.

[45] R. B. Bird, W. E. Stewart, and E. N. Lightfoot, *Transport Phenomena*, 2nd ed. Wiley, 2007.

[46] C. Wagner, "On the numerical evaluation of Fredholm integral equations with the aid of the Liouville-Neumann series," *Journal of Mathematics and Physics*, vol. 30, no. 1-4, pp. 232–234, 1951. [Online]. Available: http://dx.doi.org/10.1002/sapm1951301232

[47] M. R. Jolly and J. Q. Sun, "Passive tuned vibration absorbers for sound radiation attenuation from panels," *North American Conference on Smart Structures and Materials*, pp. 194–201, 1994.

[48] R. I. Wright and M. R. F. Kidner, "Vibration absorbers: A review of applications in interior noise control of propeller aircraft," *Journal of Vibration and Control*, vol. 10, no. 8, pp. 1221–1237, 2004.

[49] F. Jacobsen and P. M. Juhl, *Fundamentals of general linear acoustics*, 1st ed. Wiley, 2013.

[50] F. Fahy and P. Gardonio, *Sound and Structural Vibration: Radiation, Transmission and Response*, 2nd ed. Elsevier, 2007.

[51] D. S. Weaver and T. E. Unny, "The hydroelastic stability of a flat plate," *Journal of Applied Mechanics*, vol. 37, no. 3, pp. 823–827, 1970.

[52] J. Dugundji, E. Dowell, and B. Perkin, "Subsonic flutter of panels on continuous elastic foundations," *AIAA Journal*, vol. 1, no. 5, pp. 1146–1154, 1963.

[53] C. Fox, *An introduction to the calculus of variations*. Courier Corporation, 1950.

[54] D. Young and R. P. Felgar, "Tables of characteristic functions representing normal modes of vibration of a beam," *University of Texas at Austin Bulletins and Publications*, no. 4913, 1949.

[55] R. C. Dorf and R. H. Bishop, *Modern control systems*. Pearson, 2011.

[56] A. V. G. Cavalieri, W. R. Wolf, and J. W. Jaworski, "Numerical solution of acoustic scattering by finite perforated elastic plates," *Proceedings of the Royal Society A*, vol. 472, no. 2188, 2016, 20150767.

[57] M. S. Howe, "Edge-source acoustic Green's function for an airfoil of arbitrary chord, with application to trailing-edge noise," *The Quarterly Journal of Mechanics and Applied Mathematics*, vol. 54, no. 1, pp. 139–155, 2001.

[58] ——, "On the added mass of a perforated shell, with application to the generation of aerodynamic sound by a perforated trailing edge," *Proceedings of the Royal Society of London A: Mathematical, Physical and Engineering Sciences*, vol. 365, no. 1, pp. 209–233, 1979.

[59] ——, *Theory of vortex sound*. United Kingdom: Cambridge University Press, 2003.

[60] A. V. Cavalieri, W. R. Wolf, and J. W. Jaworski, "Acoustic scattering by finite poroelastic plates," in *20th AIAA/CEAS Aeroacoustics Conference*. Paper AIAA 2014-2459, 2014.

[61] L. J. Ayton, "Acoustic scattering by a finite rigid plate with a poroelastic extension," *Journal of Fluid Mechanics*, vol. 791, pp. 414–438, 2016.

[62] S. M. Patrik, C. M. Davis, and H. M. Atassi, "The acoustic directivity from airfoils in nonuniform subsonic flow," *Master Thesis, University of Notre Dame*, 1993.

[63] E. Reissner, "On the application of mathieu functions in the theory of subsonic compressible flow past oscillating airfoils," *NACA-TN 2363*, 1951.

[64] J. M. R. Graham, "Lifting surface theory for the problem of an arbitrarily yawed sinusoidal gust incident on a thin aerofoil in incompressible flow," *Aeronautical Quarterly*, vol. 21, no. 2, pp. 182–198, 1970.

Biography

Rozhin Hajian received the B.Sc. degree in Chemical engineering from Sharif University of Technology (SUT), Tehran, Iran, in 2011, M.Sc. degree in Mechanical engineering from Lehigh University, Bethlehem, PA, in 2014, and Ph.D. degree in mechanical engineering from Lehigh University in May 2018. She was an exchange student with the Department of Chemical engineering, Tokyo Institute of Technology, Japan, from 2009 to 2010, and also a visiting graduate student at Boston University, summer 2017. Moreover, she was awarded Advani Fellowship (2012), Biosystems Dynamics Summer Institute graduate fellowship (2015), Rossin Doctoral Fellowship (2016), the Graduate Student Life Leadership Award (2016), and the Graduate Student Merit Award (2018) at Lehigh University.